



On phase equilibria and crystal structures in the systems Ce–Pd–B and Yb–Pd–B. Physical properties of $R_2Pd_{13.6}B_5$ ($R=Yb, Lu$)[☆]

Oksana Sologub^a, Peter Rogl^{a,*}, Leonid Salamakha^b, Ernst Bauer^b, Gerfried Hilscher^b, Herwig Michor^b, Gerald Giester^c

^a Institute of Physical Chemistry, University of Vienna, A-1090 Wien, Währingerstrasse 42, Austria

^b Institute of Solid State Physics, Vienna University of Technology, A-1040 Wien, Austria

^c Institute of Mineralogy and Crystallography, University of Vienna, Althanstr. 14, A-1090 Wien, Austria

ARTICLE INFO

Article history:

Received 12 December 2009

Received in revised form

11 February 2010

Accepted 20 February 2010

Available online 26 February 2010

Keywords:

Phase diagram

Crystal structure

X-ray powder and single crystal diffraction

Rare earth intermetallics

Crystal chemistry of intermetallics

Physical properties of $Yb_2Pd_{13.6}B_5$

ABSTRACT

Phase equilibria and crystal structures of ternary compounds were determined in the systems Ce–Pd–B and Yb–Pd–B at 850 °C in the concentration ranges up to 45 and 33 at% of Ce and Yb, respectively, employing X-ray single crystal and powder diffraction. Phase relations in the Ce–Pd–B system at 850 °C are governed by formation of extended homogeneity fields, τ_2 -CePd₈B_{2–x} ($0.10 < x < 0.48$); τ_3 -Ce₃Pd_{25–x}B_{8–y} ($1.06 < x < 1.87$; $2.20 < y < 0.05$), and CePd₃B_x ($0 < x < 0.65$) the latter arising from binary CePd₃. Crystallographic parameters for the new structure type τ_2 -CePd₈B_{2–x} (space group C2/c, $a=1.78104(4)$ nm, $b=1.03723(3)$ nm, $c=1.16314(3)$, $\beta=118.515(1)^\circ$ for $x=0.46$) were established from X-ray single crystal diffraction. The crystal structures of τ_2 -CePd₈B_{2–x} and τ_3 -Ce₃Pd_{25–x}B_{8–y} are connected in a crystallographic group–subgroup relationship. Due to the lack of suitable single crystals, the novel structure of τ_1 -Ce₆Pd_{47–x}B₆ ($x=0.2$, C2/m space group, $a=1.03594(2)$ nm, $b=1.80782(3)$ nm, $c=1.01997(2)$ nm, $\beta=108.321(1)^\circ$) was determined from Rietveld refinement of X-ray powder diffraction data applying the structural model obtained from single crystals of homologous La₆Pd_{47–x}B₆ ($x=0.19$) (X-ray single crystal diffraction, new structure type, space group C2/m, $a=1.03988(2)$ nm, $b=1.81941(5)$ nm, $c=1.02418(2)$ nm, $\beta=108.168(1)^\circ$).

The Yb–Pd–B system is characterized by one ternary compound, τ_1 -Yb₂Pd₁₄B₅, forming equilibria with extended solution YbPd₃B_x, YbB₆, Pd₅B₂ and Pd₃B. The crystal structures of both Yb₂Pd₁₄B₅ and isotypic Lu₂Pd₁₄B₅ were determined from X-ray Rietveld refinements and found to be closely related to the Y₂Pd₁₄B₅-type (*I4₁/amd*). The crystal structure of binary Yb₅Pd_{2–x} (Mn₅C₂-type) was confirmed from X-ray single crystal data and a slight defect on the Pd site ($x=0.06$) was established.

The three structures τ_1 -Ce₆Pd_{47–x}B₆, τ_2 -CePd₈B_{2–x} and τ_3 -Ce₃Pd_{25–x}B_{8–y} are related and can be considered as the packings of fragments observed in Nd₂Fe₁₄B structure with different stacking of common structural blocks.

Physical properties for Yb₂Pd_{13.6}B₅ (temperature dependent specific heat, electrical resistivity and magnetization) yielded a predominantly Yb-4f¹³ electronic configuration, presumably related with a magnetic instability below 2 K. Kondo interaction and crystalline electric field effects control the paramagnetic temperature domain.

© 2010 Elsevier Inc. All rights reserved.

1. Introduction

The recent discovery of superconductivity in non-centrosymmetric CePt₃Si (CePt₃B-type, i.e., a tetragonally distorted variant of the CaTiO₃ perovskite type [1,2]) as well as of BCS superconductivity in MgNi₃C with anti-perovskite type [3] has stimulated intensive investigations not only in the field of perovskite intermetallics, but

has also motivated the search for novel superconducting states in related ternary or quaternary alloy systems [4,5]. Similarly, a general study of the formation of intermetallic borides and carbides AM₃X ($A=Mg, Ca, Sc, Y, Lu, Zr, Nb$; $M=Ni, Ru, Rh, Pd, Pt$ with $X=B, C$) [6] raised our interest in the R–Pd–B systems particularly for $R=Ce$, and Yb as the two systems exhibit a complementary number of electrons in the *f*-shell: one *f*-electron in Ce but one *f*-hole in Yb. Experimental studies in the systems Ce–Pd–B and Yb–Pd–B hitherto have concentrated mainly on the formation and characterization of perovskite-type compounds RPd₃B_x. Investigating the alloying behavior of boron and RPd₃ Dhar et al. [7] observed a valence transition in Ce on the insertion of boron atoms into the voids of

[☆] Dedicated to Prof. Dr. Rüdiger Kniep on the occasion of his 65th birthday

* Corresponding author. Fax: +43 1 4277 95245.

E-mail address: peter.franz.rogl@univie.ac.at (P. Rogl).

binary CePd₃. Several studies were devoted to the physical property changes in CePd₃B_x depending on boron concentration [8–10] but single crystal X-ray diffraction studies were performed only for binary CePd₃ confirming Ce atoms in the 1(*a*) site and Pd in the 3(*c*) site of the AuCu₃ type [11]. The lattice parameters reported are slightly larger than those presented by Thomson [12] for Ce- and Pd-rich members of the Ce_{1-x}Pd_{3+x} homogeneity field ($0 \leq x \leq 0.068$, $0.4129 \geq a \geq 0.4112$ nm) and agree well with the data given by Bretschneider and Schaller ($a=0.41384$ nm for $x=0.04$ within the homogeneity field $-0.012 \leq x \leq 0.048$) [13]. The insertion of boron into interstitials of the CePd₃ structure results in an increase of the unit cell and causes a non-Vergard law-like behavior of the lattice parameter variation, which was attributed to the intermediate valence of the Ce ions. Transport measurements [14] indicated that CePd₃B_x with $x \leq 0.15$ can be described as a Kondo lattice but for the samples with $x > 0.2$ the behavior was found to be completely different. It was suggested that this rearrangement is a result of the valence shift from intermediate valence at $x=0$ to a valence of 3 at $x=0.3$ [14]. For the Yb–Pd–B system, the information available for more than two decades was limited to the experimental data on the solubility of boron in YbPd₃ [7].

Recently, lattice parameters were presented for CePd₃ and “CePd₃B”, calculated in the course of DFT (density functional theory) electronic structure studies [15], although, the experimental limit of boron incorporation in perovskite-type CePd₃B_x was established at $0 < x < 0.60$ with $a=0.41935(1)$ nm for the terminal composition [2]. The above mentioned studies [15] performed by X-ray diffraction, energy dispersive and wavelength dispersive X-ray spectroscopy also questioned the existence of stoichiometric YbPd₃B reported by Dhar et al. [7] and established the limits of boron incorporation in YbPd₃B_x at $0 < x < 0.45$. The significant range of homogeneity for binary YbPd₃ ranging from YbPd_{3.44(2)} with $a=0.40317(4)$ to YbPd_{2.75(1)} with $a=0.40506(3)$ nm made an evaluation of the degree of boron filling solely based on lattice parameter investigations difficult and questionable. Moreover, within the density-functional theory using the LSDA+*U* approximation a valence instability was established for YbPd₃B_x [15], for which the authors defined an experimental maximum of boron solubility of 11 at% B ($x=0.45$) at 1000 °C.

In our search for novel materials with strong electron correlations among rare earth metal–palladium–boride systems we herein extended our studies to Ce(Yb)–Pd–B in the Ce(Yb)–poor region. Recently, we reported on structural and physical properties for a new series of palladium-rich compounds, M₂Pd_{14+x}B_{5-y} ($M=Th, La, Ce, Pr, Nd, Sm, Eu, Gd$) [16] and on the crystal structures of {La,Ce}₃Pd_{25-x}B_{8-y} [17]. Aims of the present research are devoted to (i) a detailed investigation of phase relations in the system Ce–Pd–B and Yb–Pd–B up to 45 at% Ce and 34 at% Yb, and (ii) evaluation of the crystal structures of ternary compounds in {Ce,Yb}–Pd–B and in the related systems with lutetium.

2. Experimental

All samples, each of a total amount of ca. 0.5 g, were prepared by argon arc-melting ingots of rare earths (Alfa Aesar, purity > 99.9 mass%), palladium foil (Ögussa, 99.9%) and crystalline boron (Alfa Aesar, 98%). For homogeneity, the samples were re-melted several times. A part of each alloy was wrapped in Mo-foil, sealed in an evacuated silica tube and heat-treated for 10 days at 850 °C prior to quench by submerging the capsules in cold water. Alloys within the ternary concentration field 24Ce:76Pd–12Ce:88Pd–10Ce:76Pd:14B were annealed for 4 weeks at 850 °C. X-ray powder diffraction data were collected employing a Guinier–Huber image plate system with monochromatic CuK α_1 radiation ($8^\circ < 2\theta < 100^\circ$) from as-cast and annealed alloys. Alternatively, because significant broadening of

diffraction lines was induced by the powdering process, the powders of alloys with a content of 77–82 at% Pd were placed in molybdenum containers, sealed in evacuated silica capsules and strain relieved for 30 min at 850 °C and quenched. Precise lattice parameters were calculated by least squares fits to the indexed 2θ values calibrated with Ge as internal standard ($a_{\text{Ge}}=0.565791$ nm). Single crystals were mechanically isolated from the crushed as-cast and annealed alloys. Inspections on an AXS-GADDS texture goniometer assured high crystal quality, unit cell dimensions and monoclinic Laue symmetry of the specimens prior to X-ray intensity data collections on a four-circle Nonius Kappa diffractometer equipped with a CCD area detector employing graphite monochromated MoK α radiation ($\lambda=0.071069$ nm). Orientation matrices and unit cell parameters were derived using the program DENZO [18]. No absorption corrections were performed because of the rather regular crystal shapes and small dimensions of the investigated specimens. The structures were solved by direct methods and were refined with the SHELXL-97 program [19,20]. Quantitative Rietveld refinements of the X-ray powder diffraction data were performed with the FULLPROF program [21]. Measurements of the various physical properties were carried out with a series of standard techniques for which details can be inquired from Ref. [4].

3. Results and discussion

3.1. Binary systems

The crystal data relevant to the unary and binary boundary phases in the Ce–Pd–B and Yb–Pd–B systems are listed in Table 1. Although several research groups have dealt with the phase relations in the Ce–Pd system, there is still severe controversy among the various versions of the phase diagram [12,13,24]. This problem has not yet been resolved satisfactorily in the most recent critical assessment by Okamoto [25]. Discrepancies mainly concern (a) the stability range of CePd₇, which for this work we take from Bretschneider [13] and (b) the crystal structure of Ce₃Pd₅, which as already mentioned by Thomson [12] does not correspond to the Th₃Pd₅ structure. In agreement with a recent study of Ce–Pd–Si [26], only the two cubic phases, CePd₃ and CePd₅ [27], were found at 850 °C in the concentration region from 75 to 83 at% Pd.

The phase diagram Yb–Pd was assessed by Okamoto [25]. A recent study [15] established the limits of the YbPd₃ homogeneity field extending from YbPd_{3.44(2)} to YbPd_{2.75(1)} at 800 °C. Within our present cursory investigation X-ray powder data were analyzed for several Yb–Pd alloys both in annealed and in as-cast conditions and were found to be consistent with data in literature. As a single crystal of good quality was found from the as-cast alloy Yb₅Pd₂ the crystal structure was refined particularly as hitherto only isotypism with the structure type of Mn₅C₂ has been stated from X-ray photographs [38]. The structure refinement ($R^2=0.035$) confirmed the Mn₅C₂-type with a small defect in one of the Pd-sites, which is occupied for 96.9(4)% only, leading to an overall composition Yb₅Pd_{1.94}. Results are compiled in Table 2. The Pd–B system used herein is from a reinvestigation by the authors [40]. The low-temperature ordering phases in the Pd-rich region [41] are not relevant for the phase relations of the {Ce,Yb}–Pd–B ternary systems at 850 °C. Both Ce–B and Yb–B binary phase diagrams are accepted in the versions presented by Massalski [22].

3.2. Ce–Pd–B system

3.2.1. Crystal structure of La₆Pd_{47-x}B₆ ($x=0.19$) and τ_1 -Ce₆Pd_{47-x}B₆ ($x=0.2$)

The X-ray phase analysis of Ce–Pd–B alloys revealed a compound with hitherto unknown structure in the proximity of

Table 1
Crystallographic data of unary and binary boundary phases and ternary compounds of the systems Ce(Yb)–Pd–B.

Phase, temperature range (°C)	Space group, prototype	Lattice parameters (nm)			Comments
		<i>a</i>	<i>b</i>	<i>c</i>	
(γ)Ce 798–726 [22]	$Im\bar{3}m$ W	0.412	–	–	[23]
(γ)Yb 819–795 [22]	$Im\bar{3}m$ W	0.444	–	–	[23]
(β)Yb < 795 [22]	$Fm\bar{3}m$ Cu	0.5485	–	–	[23]
(Pd) < 1555 [22]	$Fm\bar{3}m$ Cu	0.38903	–	–	[23]
Ce_xPd_{1-x} [13]	$Fm\bar{3}m$ Cu	0.38902–0.39775 0.38941 0.39060 0.39229 0.39295 0.39400 0.39775	–	–	$0 \leq x \leq 0.067$ at 1000 °C [13] $x=0.002$ [13] $x=0.013$ [13] $x=0.025$ [13] $x=0.030$ [13] $x=0.040$ [13] $x=0.068$ (Pd)+ $Ce_{1-x}Pd_{7+x}$ [13]
Yb_xPd_{1-x} < 1555 [25]	$Fm\bar{3}m$ Cu	– 0.3890–0.3965 0.3890–0.3935	–	–	$0 \leq x \leq 0.165$ at 900 °C [33] $0 \leq x \leq 0.12$ [34] $0 \leq x \leq 0.08$ [35]
PdB_x [40] PdB_x (β B) < 2092 [22]	$Rm\bar{3}m$ β B	– 0.39913–0.40040 1.09251	–	–	$0 \leq x \leq 0.195$ at 850 °C [40] for $0.144 \leq x \leq 0.177$ [41] [23]
β - $Ce_{1-x}Pd_{7+x}$ 1543–600 [13]	$Fm\bar{3}m$ CuPt ₇	– 0.8127–0.7955 0.79550 0.79688 0.80805 0.81221 0.81266	–	–	[28] $-0.024 < x \leq 0.184$ at 1000 °C [13] $x=0.184$ [13] $x=0.168$ [13] $x=0.040$ [13] $x=-0.016$ [13] $x=-0.024$, $CePd_7+CePd_5$ [13] $-0.016 < x < 0.168$ at 550 °C [13]
α - $Ce_{1-x}Pd_{7+x}$ < 600 [13]	<i>h</i>	– 0.2596 0.2594 0.2593 0.4055	–	–	$-0.016 < x < 0.168$ at 550 °C [13] $x=0.168$ $Ce_xPd_{1-x}+Ce_{1-x}Pd_{7+x}$ [13] $x=0.04$ [13] $x=-0.0156$ $Ce_{1-x}Pd_{7+x}+Ce_{1-x}Pd_{3+x}$ [13] at 1000 °C [13]
$CePd_5$ 1348–1060 [13]	<i>c</i>	0.4055	–	–	
β - $CePd_5$ 1180–801 [24]	<i>h</i>	–	–	–	[24]
α - $CePd_5$ [24] < 600 [27]	<i>c</i> <i>Pmma</i> <i>c</i>	– 0.57004 0.4056	– 0.40622	–	< 801 °C [24] [27] > 700 °C [27]
$CePd_5$ [29]	$P6/mmm$ CaCu ₅	0.5373	–	0.4177	[29]
$Ce_{1-x}Pd_{3+x}$ < 1437 [12]	$Pm\bar{3}m$ AuCu ₃	0.4129–0.4112 –	–	–	– $0 \leq x \leq 0.068$ [12] at 800 °C
$Ce_{1-x}Pd_{3+x}$ [32]		0.41384 0.41231(1)–0.41131(9)	–	–	$-0.012 \leq x \leq 0.048$ [13] $x=0.04$ [13] at 850 °C [this work]
$CePd_3B_y$ –	$Pm\bar{3}m$ CaTiO ₃	– 0.41935(1)	–	–	$0 \leq y \leq 0.60$ at 800 °C [2] for $y=0.60$ [2]
$Ce_{1-x}Pd_{3+x}B_y$		0.41694(4) 0.41954(5)	–	–	$y=0.125$ at 850 °C (this work) $y=0.25$ at 850 °C (this work)
Ce_3Pd_5 < 1037 [22]	<i>P-62m</i> Th ₃ Pd ₅ unknown	0.725 –	–	0.385 –	[30] – [12, this work]
Ce_3Pd_4 < 1130 [22]	$R\bar{3}m$ Pu ₃ Pd ₄	1.3669	–	0.5824	[31]
YbPd ₇ < 448 [25]		–	–	–	[34]
$Yb_{1-x}Pd_{3+x}$ < 1700 [38]	$Pm\bar{3}m$ AuCu ₃	– 0.40317 0.4054–0.4040 0.40506–0.40317	–	–	$0 \leq x \leq 0.16$ [25] for $x=0$ at 900 °C [36,37] [38] $-0.067 \leq x \leq 0.099$ [15]
$YbPd_{2.99(2)}B_x$ [7]	$Pm\bar{3}m$ CaTiO ₃	0.4050–0.4088 – 0.40938(2) 0.40990(5)	–	–	$0 \leq x \leq 1$ [7] $0 \leq x \leq 0.45$ [15] for $x=0.45(1)$ [15] for $x=0.45$, multiphase alloy (this work)
β -YbPd ₂ 1382–1135 [38]		–	–	–	[38] –

Table 1 (continued)

Phase, temperature range (°C)	Space group, prototype	Lattice parameters (nm)			Comments
		a	b	c	
α -Yb _{1-x} Pd _{2+x} < 1135 ³⁴					x=0.041 [38]
β -Yb ₃ Pd ₅ 1360–1165 [38]					[38]
α -Yb ₃ Pd ₅ < 1155 [38]					
Yb ₃ Pd ₄ < 1415 [38]	$R\bar{3}m$ Pu ₃ Pd ₄	1.2900		0.5654	[38]
β -Yb _{1-x} Pd _x 1460–1435 [38]	$Pnma$ FeB	0.7220	0.4123	0.5578	0 ≤ x ≤ 0.06 [22,23]
α -YbPd < 1435 [38]	$Pm\bar{3}m$ CsCl	0.3440			0 ≤ x ≤ 0.06 [39]
β -Yb ₅ Pd ₂ 695–685 [38]	–	–	–	–	[38]
α -Yb ₅ Pd ₂ < 685 [38]	$C2/c$ Mn ₅ C ₂	1.6321	0.6550	0.7680	[38]
Yb ₅ Pd _{2-x}	$C2/c$ Mn ₅ C ₂	1.63188(7)	0.65678(3) β=97.53°	0.76506(3)	x=0.06 (this work)
Yb ₃ Pd < 670 [38]	$Pnma$ Fe ₃ C	0.7664	0.9678	0.6500	[38]
Pd ₄ B 1138–933 [40]					[40,23]
Pd ₃ B < 1125 [40]	$Pnma$ Fe ₃ C	0.5463	0.7567	0.4852	[40,23]
Pd ₅ B ₂ < 1077 [40]	$C2/c$ Mn ₅ C ₂	1.2786	0.4955	0.5472	[40,23]
Pd ₂ B < 994 [40]	$Pnmm$ CaCl ₂	0.46918	0.51271	0.31096	[40,23]
CeB ₆ < 2550 [22] < 2330 [25]	$Pm\bar{3}m$ CaB ₆	0.41396			[23]
CeB ₄ < 2380 [22] < 2165 [25]	$P4/mbm$ UB ₄	0.7206		0.4090	[25] [23]
YbB ₆ < 2150 [22]	$Fm\bar{3}c$ YB _{65.86}	0.23422			[23]
YbB ₁₂ < 2200 [22]	$Fm\bar{3}m$ UB ₁₂	0.7468			[23]
YbB ₆ < 2300 [22]	$Pm\bar{3}m$ CaB ₆	0.41479			[23]
Yb _{1-x} B _{6+x}		–			0 ≤ x ≤ 0.06 (this work)
YbB ₄ < 1850 [22]	$P4/mbm$ UB ₄	0.4127 – 0.4147 0.7064		0.3989	at 850 °C (this work) [23]
YbB ₂ < 1500 [22]	$P6/mmm$ AlB ₂	0.32503		0.37315	[23]
Ce ₆ Pd _{47-x} B ₆	$C2/m$ La ₆ Pd _{47-x} B ₆	1.03594(2)	1.80782(3) β=108.321(1)°	1.01997(2)	x=0.19 at 850 °C (this work)
CePd ₈ B _{2-x}	$C2/c$ CePd ₈ B _{2-x}	–	–	–	0.08 < x < 0.48 at 850 °C (this work)
		1.7790(3)	1.0349(1) β=118.54	1.1708(2)	boron rich (this work)
		1.7803(1)	1.03601(4) β=118.75	1.16152(6)	boron poor (this work)
Ce ₃ Pd _{25-x} B _{8-y}	$P2_1/c$ La ₃ Pd _{25-x} B _{8-y}	–	–	–	1.06 < x < 1.88; 2.20 < y < 0.05 at 850 °C (this work)
		1.17274(3)	1.05537(2) β=102.265(1)°	1.60271(4)	boron rich (this work)
		1.1734(4)	1.0455(2) β=102.13(1)°	1.5966(5)	boron poor (this work)
Yb ₂ Pd _{13.6} B ₅	$I4_1/amd$ Nd ₂ Pd _{14+x} B _{5-x} -related	0.83812(2)		1.66034(5)	(this work)

the composition 10Ce:80Pd:10B. Due to incongruent melting a suitable single crystal specimen was only obtained from a homologous La-containing alloy. The crystal showed monoclinic Laue symmetry $2/m$ with systematic extinctions compatible with space group $C2/m$ (no. 12). The initial atomic positions of

La and Pd atoms were deduced from direct methods, boron atoms were located from difference Fourier synthesis. The difference electron density map revealed additional peaks, which were considered as split sites for Pd3 and Pd10. When allowed to refine freely, the occupancies converged to 0.927Pd3/0.073Pd3a and

Table 2Crystal structure data^a for Yb₅Pd_{2-x} (x=0.06) and R₂Pd_{14-x}B₅ compounds (R=Yb, Lu).

Nominal composition	Yb _{72.1} Pd _{27.9}	Yb _{9.7} Pd _{66.0} B _{24.3}	Lu _{9.9} Pd _{65.3} B _{24.8}				
Space group	C2/c; no. 15	I4 ₁ /amd; no. 141	I4 ₁ /amd; no. 141				
Structure type	Mn ₅ C ₂	Y ₂ Pd ₁₄ B ₅ -related	Y ₂ Pd ₁₄ B ₅ -related				
Formula from refinement	Yb ₅ Pd _{1.94}	Yb ₂ Pd _{13.6} B ₅	Lu ₂ Pd _{13.2} B ₅				
Diffractometer	Nonius KappaCCD, MoK α	Guinier–Huber image plate, CuK α ₁	Guinier–Huber image plate, CuK α ₁				
Theta range	3.35° < 2 θ < 72.54°	8° < 2 θ < 100°	8° < 2 θ < 100°				
Crystal size	35 × 35 × 15 μ m ³	–	–				
a (nm)	1.63188(7)	0.83812(2)	0.84173(4)				
b (nm)	0.65678(3)	–	–				
c (nm)	0.76506(3)	1.66034(5)	1.65761(8)				
β (deg)	97.317(2)	–	–				
Reflections in refinement	1456 F _o > 4 σ (F _o) of 1905	216	218				
Mosaicity	< 0.4	–	–				
Number of variables	35	31	31				
Reliability factors	R _F ² = $\Sigma F_o^2 - F_c^2 /\Sigma F_o^2 = 0.035$;	R _F = $\Sigma F_o - F_c /\Sigma F_o = 0.033$	R _F = $\Sigma F_o - F_c /\Sigma F_o = 0.073$				
–	–	R _I = $\Sigma I_o - I_c /\Sigma I_o = 0.045$	R _I = $\Sigma I_o - I_c /\Sigma I_o = 0.062$				
–	R _{int} = 6.6	R _{exp} = $[(N - P + C)/\Sigma w_i y_{oi}^2]^{1/2} = 1.05$	R _{exp} = $[(N - P + C)/\Sigma w_i y_{oi}^2]^{1/2} = 1.10$				
GOF	0.797	$\chi^2 = (R_{wp}/R_e)^2 = 33.6$	$\chi^2 = (R_{wp}/R_e)^2 = 9.2$				
Extinction (Zachariasen)	0.00000(6)	–	–				
R1;	8f (x,y,z); x=0.21854(2), y=0.08127(6), z=0.31712(5)	8e (0,1/4,z); z=0.0958(1)	8e (0,1/4,z); z=0.0953(1)				
Occ., U _{eq} (B _{iso}) ^b	1.00 Yb, 0.01833(13)	1.00 Yb, 0.97(7)	1.00 Lu, 0.88(9)				
R2;	8f (x,y,z), x=0.40865(3), y=0.11467(6), z=0.07897(5)	–	–				
Occ., U _{eq}	1.00 Yb, 0.01981(13)	–	–				
R3;	4e (0,y,1/4), y=0.08445(8)	–	–				
Occ., U _{eq}	1.00 Yb, 0.01616(14)	–	–				
Pd1;	8f(x,y,z), x=0.10876(5), y=0.20415(12), z=0.57881(9)	16h (0,y,z); y=0.0367(2), z=0.2366(1)	16h (0,y,z); y=0.0340(2), z=0.2407(1)				
Occ., U _{eq} (B _{iso})	0.969(4) Pd, 0.01958(22)	1.00 Pd, 0.85(6)	1.00 Pd, 0.14(9)				
Pd2;	–	16h (0,y,z); y=0.5861(2), z=0.0667(1)	16h (0,y,z); y=0.5917(2), z=0.0644(1)				
Occ., B _{iso}	–	1.00 Pd, 0.35(6)	1.00 Pd, 0.78(9)				
Pd3;	–	16g (x,x+1/4,7/8); x=0.2922(2)	16g (x,x+1/4,7/8); x=0.2969(2)				
Occ., B _{iso}	–	0.92(2) Pd, 0.77(6)	0.80(2) Pd, 0.83(11)				
Pd4; Occ., B _{iso}	–	8d (0,0,1/2); 1.00 Pd, 0.81(9)	8d (0,0,1/2); 1.00 Pd, 0.98(10)				
B1; Occ. ^c , B _{iso} ^c	–	16f (x,0,0); x=0.204(2); 1.00B,0.80	16f (x,0,0); x=0.204(2); 1.00B,0.80				
B2; Occ. ^c , B _{iso} ^c	–	4b (0,1/4,3/8); 1.00 B, 0.80	4b (0,1/4,3/8); 1.00 B, 0.80				
Residual density; max; min (e _l /nm ³) × 10 ³	4.032; –2.342	–	–				
Interatomic distances in [10 nm] for Yb ₅ Pd _{1.94} (Mn ₅ C ₂ -type, space group C2/c; no. 15)							
Yb1–Pd4	2.9635(8)	Yb1–Yb2	4.1992(6)	Yb2–Pd4	3.4758(10)	Yb3–2Yb2	3.6630(5)
Yb1–Pd4	3.0357(8)			Yb2–Yb3	3.9452(6)	Yb3–2Yb2	3.9452(6)
Yb1–Pd4	3.1608(8)	Yb2–Pd4	2.9225(8)	Yb2–Yb1	3.9846(6)	Yb3–2Yb3	3.9829(3)
Yb1–Yb3	3.5379(4)	Yb2–Pd4	2.9530(9)	Yb2–Pd4	4.0546(9)	Pd4–2Yb2	2.9225(8)
Yb1–Yb1	3.6146(8)	Yb2–Yb3	3.5996(6)	Yb2–2Yb2	4.1112(6)	Pd4–Yb1	2.9636(9)
Yb1–2Yb1	3.6279(4)	Yb2–Yb3	3.6630(5)	Yb2–Yb1	4.1992(6)	Pd4–Yb3	2.9932(8)
Yb1–Yb2	3.7028(6)	Yb2–Yb2	3.6791(7)			Pd4–Yb3	3.0084(9)
Yb1–Yb2	3.7990(6)	Yb2–Yb1	3.7028(6)	Yb3–2Pd4	2.9932(8)	Pd4–Yb1	3.0357(9)
Yb1–Yb2	3.8408(6)	Yb2–Yb2	3.7081(6)	Yb3–2Pd4	3.0084(9)	Pd4–Yb1	3.1609(9)
Yb1–2Yb1	3.9714(3)	Yb2–Yb1	3.7990(6)	Yb3–2Yb1	3.5378(4)	Pd4–Yb2	3.4758(10)
Yb1–Yb2	3.9846(6)	Yb2–Yb1	3.8408(6)	Yb3–2Yb2	3.5996(6)	Pd4–Yb2	4.0546(9)

^a Crystal structure data are standardized using the program Structure Tidy [42].^b Atomic displacement parameters are given in [10² nm²].^c Fixed parameters.

0.927Pd10/0.072Pd10a constraining each split site to a total occupancy of $\text{occ}(\text{Pd3}+\text{Pd3a})=1$ and $\text{occ}(\text{Pd10}+\text{Pd10a})=1$. All other sites were found to be fully occupied except for Pd16 ($\text{occ } 0.82$), which is located too close to Pd3a and Pd10a. The split positions as well as the boron atoms were refined with isotropic displacement parameters. A subsequent difference Fourier synthesis revealed no significant residual peaks (residual electron density < 4.2 (e.l./nm³) $\times 10^3$ at 0.070 nm from Pd9; see Table 3). Space groups of lower symmetry (*Cm*, *C2*, *P2/m*, *Pm*, *P2* and *P-1*) were tested to ascertain if the disorder problems result from an incorrect choice of space group with too high symmetry. In all cases, the same features of split palladium sites persist and careful re-examination of the CCD frames of the intensity data provided no signs of superstructure reflections.

The distances between atoms and coordination polyhedra are presented in Supplementary Data in Table 1 and in Fig. 1, respectively. Due to split atomic sites (Pd3/Pd3a and Pd10/Pd10a), which cannot be simultaneously occupied, two drawings of coordination shells are shown for the atoms in contact. The coordination polyhedra around both La sites are well defined. La1 is surrounded only by palladium atoms, whereas the coordination sphere of La2 includes, besides 17 palladium atoms, one boron atom located against the rectangular face. Typically for rare earth intermetallics with high metal content (Th₆Mn₂₃, Mg₂Zn₁₁), the coordination polyhedra for lanthanum atoms (CN 17 and 18 for La1 and La2, respectively) can be deduced from the combination of pentagonal prisms and pentagonal pyramids. The coordination numbers for palladium atoms vary from CN 10 (cube with two additional atoms for Pd16) to CN 16 for Pd13; in most cases, the coordination shells for Pd atoms are icosahedra or their derivatives. The split atom sites, Pd3a and Pd10a, which are occupied by 7.3% and 7.2% each are coordinated by 11 atoms exhibiting shortened distances to certain neighboring atoms (e.g., Pd3a–La2 0.2896(7) nm; Pd3a–Pd10a 0.2083(8) nm; Pd3a–Pd3a 0.2031(7) nm). Analysis of interatomic distances also showed that the proximity of the Pd3, Pd10 and Pd16 atomic sites to those of Pd3a and Pd10a precludes these positions from being simultaneously occupied.

Two borons are coordinated by 7 (for B1) and 9 (for B2) metal atoms. B1 is not placed exactly in the center of the triangular palladium prism; it is shifted in *b* direction towards the rectangular face thus forming an additional contact with the neighboring palladium atom. The Archimedean antiprism is capped with one lanthanum atom displaying a large distance $d_{\text{B-La}}=0.3252(12)$ nm.

The complicated structure model obtained from the La-single crystal was confirmed by Rietveld analysis of the X-ray powder data for the Ce-isotope (Table 3, Fig. 1) exhibiting low residual values and good agreement between calculated and observed intensities. The X-ray powder diffraction spectrum taken from the 11Ce:79.5Pd:10.5B alloy resembled, in addition to the complex pattern of τ_1 , small amounts of foreign cubic phases for which only the main reflections were detectable (Fig. 1, middle and low rows of Bragg's positions correspond to diffraction peaks from unknown cubic phases; see also Table 6).

Fig. 2 shows the projections of the structure La₆Pd_{47-x}B₆ ($x=0.191$) onto [001], [010] and [100] planes. The structure can be considered as an arrangement of slabs in which four types of polyhedra centered by Pd (Pd14 in 4f (1/4,1/4,1/2); Pd15 in 2d (0,1/2,1/2); Pd16 in 2c (0,0,1/2) and Pd17 in 2a (0,0,0)) and two types of polyhedra centered by boron (B1 in 8j (*x,y,z*) $x=0.3588(7)$, $y=0.1796(4)$, $z=0.1056(7)$; B2 in 4i (*x,0,z*); $x=0.4019(10)$, $z=0.0913(11)$) are packed such as to nearly occupy the entire unit cell leaving unfilled voids with dimensions too small to house an additional atom.

3.2.2. Crystal structure of CePd₈B_{2-x}

X-ray structure determinations were performed for two crystals selected from as-cast and annealed alloys with different content of boron within the homogeneity field ($x_1=0.46$, $x_2=0.32$). The intensity patterns of both crystals indicated monoclinic Laue symmetry and systematic extinctions, $h+k=2n$ for (*hkl*) and $l=2n$ for (*h0l*), consistent with the *C*-centered space groups *Cc* and *C2/c*. Intensity statistics favored the centrosymmetric space group *C2/c*. Direct methods established the initial positions of the Ce and Pd atoms. The atomic positions of boron atoms were located from difference Fourier synthesis. The structures were refined by full-matrix least-squares methods on F^2 with anisotropic displacement parameters for Ce and Pd atoms but isotropic temperature factors for boron atoms (Table 4). Refinements on the occupancy factors confirmed that in both crystals all the sites are fully occupied except for atom site B2 and thus resulted in the formulae CePd₈B_{1.54} and CePd₈B_{1.68}. Final difference Fourier maps revealed residual peaks as low as 2.81 and 4.13 (e.l./nm³) $\times 10^3$, respectively. All atomic sites exhibit reasonable atom displacement parameters except Pd12 for which the thermal ellipsoid is elongated towards *c*-direction and can be explained by the unusual coordination within the large distorted tri-capped hexagonal antiprism with rather long distances 0.27595(6) nm to the closest two neighboring Pd2 atoms (Fig. 3). For interatomic distances, the readers are kindly referred to Table 2 in Supplementary Data. All remaining 12 palladium atoms are in 12- to 16-fold coordination exhibiting rather tight bonding with a shortest contact distance $d_{\text{Pd11-Pd13}}=0.25588(5)$ nm (Fig. 4). The large Ce atoms occupy two atomic sites, both with high coordination numbers of 18 (Ce1) and 17 (Ce2). The Ce2 atom has only palladium neighbors. Ce–Pd distances cover the range between $d_{\text{Ce1-Pd3}}=0.30130(6)$ nm and $d_{\text{Ce2-Pd10}}=0.361(6)$ nm. There are only three boron positions, all showing a trigonal-prismatic coordination as typical for compounds of low-boron content. The rectangular faces of the B3-centered prisms are capped with one Pd-atom. The distorted triangular prisms centered by B1 and B2 also exhibit two and three additional atoms around the waist of the rectangular faces thus rendering the coordination geometry close to squared antiprismatic. The triangular prisms with B1 and B3 are paired via common edges, and the coupling of B2 coordination polyhedra is realized via rectangular faces. In agreement with the classification of boride structure types based on the type of boron–boron aggregation as a function of metal–boron ratio [43], no boron–boron contacts were observed in the structure (Table 2, Supplementary Data).

As observed from X-ray Rietveld refinements, the CePd₈B_{2-x} phase (*C2/c* space group) exists at 850 °C within the concentration region from 14 at% B to 17.5 at% B. The single crystal data (CePd₈B_{1.54}, CePd₈B_{1.68}) show that the increase of boron content in the structure is realized via an increase of the occupancy in the B site. On reaching 17.5 at% B, the phase Ce₃Pd_{25-x}B_{8-y} with space group *P2₁/c* is formed which exhibits partly occupied positions for certain palladium atoms as well as vacant B atom sites (crystal with 18.2 at% B [17]). Further boron increase in the structure which finally terminates at the boron-rich end of the homogeneity field at 23 at% B (at 850 °C) is possible due to filling vacant atomic positions with boron and by simultaneously diminishing the occupancy of partly filled palladium sites.

3.2.3. Crystal structure of the boron-rich end of the homogeneity field Ce₃Pd_{25-x}B_{8-y}

Attempts to establish (i) the upper boron limit of the homogeneity field of Ce₃Pd_{25-x}B_{8-y} and (ii) to estimate the mechanism of boron uptake by the structure suffered from

Table 3
Crystal structure data for $R_6Pd_{47-x}B_6$ ($R=La, Ce$; new structure type, $C2/m$ space group).

Nominal composition	$La_{10.2}Pd_{79.6}B_{10.2}$	$Ce_{10.2}Pd_{79.6}B_{10.2}$
Structure type	$La_6Pd_{47-x}B_6$	$La_6Pd_{47-x}B_6$
Formula from refinement	$La_6Pd_{47-x}B_6$ ($x=0.19$)	$Ce_6Pd_{47-x}B_6$ ($x=0.2$)
Range for data collection	$2.09 < \theta < 36.30$	$8^\circ < 2\theta < 100^\circ$
Crystal size	$45 \times 35 \times 35 \mu m^3$	Guinier–Huber image plate, $CuK\alpha_1$
<i>a</i> (nm)	1.03988(2)	1.03594(2)
<i>b</i> (nm)	1.81941(5)	1.80782(3)
<i>c</i> (nm)	1.02418(2)	1.01997(2)
β (deg)	108.168(1)	108.321(1)
Reflections in refinement	3173 $F_o > 4\sigma(F_o)$ of 4449	1093
Mosaicity	< 0.4	–
Number of variables	151	106
$R_F^2 = \sum F_o^2 - F_c^2 / \sum F_o^2$	0.0333	$R_F = \sum F_o - F_c / \sum F_o = 0.048$
–	–	$R_I = \sum I_o - I_c / \sum I_o = 0.064$
–	–	$R_{exp} = [(\sum (N - P + C) / \sum w_i y_{oi}^2)]^{1/2} = 1.06$
GOF	1.027	$\chi^2 = (R_{wp}/R_e)^2 = 14.7$
Extinction (Zachariasen)	0.00005(1)	–
$R1^a$ in 8j (<i>x, y, z</i>); occ.	0.28483(3), 0.35008(2), 0.26059(4); 1.00 La	0.2859(5), 0.3479(2), 0.2638(4); 1.0 Ce;
$U_{11}^b, U_{22}, U_{33}, U_{23}, U_{13}, U_{12};$ B_{iso}^c	0.0124(2), 0.0117(2), 0.0128(2), 0.0016(1), 0.0045(1), 0.0001(1)	– 0.87(8)
$R2$ in 4i (<i>x, 0, z</i>); occ.	0.21660(5), 0.29506(5); 1.00 La	0.2179(6), 0.2896(6); 1.0 Ce;
$U_{11}, U_{22}, U_{33}, U_{23}=U_{12}=0, U_{13};$ B_{iso}	0.0129(2), 0.0107(3), 0.0128(2), 0.0005(2)	– 0.22(9)
Pd1 in 8j (<i>x, y, z</i>); occ.	0.02363(4), 0.12318(3), 0.14335(5); 1.00 Pd	0.0238(5), 0.1242(3), 0.1369(6); 1.0 Pd;
$U_{11}, U_{22}, U_{33}, U_{23}, U_{13}, U_{12};$ B_{iso}	0.0108(2), 0.0088(2), 0.0135(2), 0.0007(1), 0.0043(2), –0.0006(2)–	– 0.61(8)
Pd2 in 8j (<i>x, y, z</i>); occ.	0.02882(4), 0.26488(3), 0.24735(5); 1.00 Pd	0.0326(5), 0.2655(3), 0.2490(5); 1.0 Pd;
$U_{11}, U_{22}, U_{33}, U_{23}, U_{13}, U_{12};$ B_{iso}	0.0106(2), 0.0124(3), 0.0107(2), –0.0009(2), 0.0031(2), 0.0009(2)	– 0.76(9)
Pd4 in 8j (<i>x, y, z</i>); occ.	0.13054(5), 0.37873(3), 0.48401(5); 1.00 Pd	0.1266(6), 0.3773(3), 0.4828(5); 1.0 Pd;
$U_{11}, U_{22}, U_{33}, U_{23}, U_{13}, U_{12};$ B_{iso}	0.0166(2), 0.0125(2), 0.0138(2), 0.0020(2), 0.0030(2), 0.0046(2)	– 0.62(8)
Pd5 in 8j (<i>x, y, z</i>); occ.	0.13589(4), 0.22913(3), 0.01870(4); 1.00 Pd	0.1336(5), 0.2286(3), 0.0216(5); 1.0 Pd;
$U_{11}, U_{22}, U_{33}, U_{23}, U_{13}, U_{12};$ B_{iso}	0.0079(2), 0.0098(2), 0.0113(2), 0.0014(2), 0.0030(2), –0.0001(1)	– 0.57(9)
Pd6 in 8j (<i>x, y, z</i>); occ.	0.23533(4), 0.08284(3), 0.02441(5); 1.00 Pd	0.2297(6), 0.0852(3), 0.0276(5); 1.0 Pd;
$U_{11}, U_{22}, U_{33}, U_{23}, U_{13}, U_{12};$ B_{iso}	0.0087(2), 0.0101(2), 0.0102(2), –0.0000(1), 0.0022(2), 0.0006(2)	– 0.89(8)
Pd7 in 8j (<i>x, y, z</i>); occ.	0.27615(4), 0.17996(3), 0.26967(4); 1.00 Pd	0.2756(6), 0.1805(3), 0.2653(5); 1.0 Pd;
$U_{11}, U_{22}, U_{33}, U_{23}, U_{13}, U_{12};$ B_{iso}	0.0115(2), 0.0123(2), 0.0089(2), –0.0001(2), 0.0035(2), 0.0010(2)	– 0.69(9)
Pd8 in 8j (<i>x, y, z</i>); occ.	0.46918(4), 0.07965(3), 0.24413(5); 1.00 Pd	0.4730(6), 0.0789(3), 0.2381(6); 1.0 Pd;
$U_{11}, U_{22}, U_{33}, U_{23}, U_{13}, U_{12};$ B_{iso}	0.0111(2), 0.0104(2), 0.0114(2), –0.0003(2), 0.0017(2), 0.0006(2)	– 0.58(8)
Pd9 in 4i (<i>x, 0, z</i>); occ.	0.09647(7), 0.77586(7); 1.00 Pd	0.0874(7), 0.7625(7); 1.0 Pd;
$U_{11}, U_{22}, U_{33}, U_{23}=U_{12}=0, U_{13};$ B_{iso}	0.0137(3), 0.0131(4), 0.0171(3), 0.0067(3)	– 0.98(14)
Pd11 in 4i (<i>x, 0, z</i>); occ.	0.61898(6), 0.11160(7); 1.00 Pd	0.6221(8), 0.1232(8); 1.0 Pd;
$U_{11}, U_{22}, U_{33}, U_{23}=U_{12}=0, U_{13};$ B_{iso}	0.0119(3), 0.0097(3), 0.0178(3), 0.0065(3)	– 0.96(12)
Pd12 in 4h (<i>0, y, 1/2</i>); occ.	0.25094(4); 1.00 Pd	0.2504(4); 1.0 Pd;
$U_{11}, U_{22}, U_{33}, U_{23}=U_{12}=0, U_{13};$ B_{iso}	0.0106(3), 0.0245(4), 0.0146(3), 0.0050(2)	– 0.95(10)
Pd13 in 4g (<i>0, y, 0</i>); occ.	0.36310(4); 1.00 Pd	0.3640(4); 1.0 Pd;
$U_{11}, U_{22}, U_{33}, U_{23}=U_{12}=0, U_{13};$ B_{iso}	0.0128(3), 0.0088(3), 0.0124(3), 0.0043(2)	– 0.98(13)
Pd14 in 4f (<i>1/4, 1/4, 1/2</i>); occ.	1.00 Pd	1.0 Pd
$U_{11}, U_{22}, U_{33}, U_{23}, U_{13}, U_{12};$ B_{iso}	0.0078(3), 0.0121(3), 0.0122(3), –0.0019(3)	– 0.69(11)
Pd15 in 2d (<i>0, 1/2, 1/2</i>); occ.	0.0032(3), 0.0018(2)	1.0 Pd
$U_{11}, U_{22}, U_{33}, U_{23}=U_{12}=0, U_{13};$ B_{iso}	0.0126(4), 0.0092(5), 0.0147(5), 0.0030(3)	– 1.1(2)
Pd16 in 2c (<i>0, 0, 1/2</i>); occ.	0.819(3) Pd	0.8 Pd

Table 3 (continued)

$U_{11}, U_{22}, U_{33}, U_{23}=U_{12}=0, U_{13};$	0.0145(6), 0.0127(6), 0.0123(6), 0.0032(4)	–
B_{iso}	–	1.2(3)
Pd17 in 2a (0,0,0); occ.	0.993(3) Pd	1.0 Pd
$U_{11}, U_{22}, U_{33}, U_{23}=U_{12}=0, U_{13};$	0.0104(4), 0.0068(5), 0.0113(5), 0.0048(3)	–
B_{iso}	–	0.23(15)
Pd3 in 8j (x,y,z); occ.	0.09015(5), 0.12396(3), 0.41902(5); 0.927(1) Pd	0.091(1); 0.119(1); 0.423(1); 0.93 Pd;
$U_{11}, U_{22}, U_{33}, U_{23}, U_{13}, U_{12};$	0.0150(2), 0.0162(3), 0.0154(3), –0.0003(2), 0.0067(2), –0.0016(2)	–
B_{iso}	–	0.47(9)
Pd3a in 8j (x,y,z); occ.	0.06589(6), 0.07934(4), 0.44472(7); 0.073(1) Pd	0.059(9), 0.122(6), 0.396(9); 0.07 Pd;
$U_{11}, U_{22}, U_{33}, U_{23}, U_{13}, U_{12};$	0.0150(2), 0.0162(3), 0.0154(3), –0.0003(2), 0.0067(2), –0.0016(2)	–
B_{iso}	–	0.47(9)
Pd10 in 4i (x,0,z); occ.	0.27211(8), 0.60882(8); 0.928(1) Pd	0.2733(9), 0.6037(10); 0.93 Pd;
$U_{11}, U_{22}, U_{33}, U_{23}=U_{12}=0, U_{13};$	0.0147(4), 0.0174(4), 0.0137(4), 0.0051(3)	–
B_{iso}	–	0.76(11)
Pd10a in 4i (x,0,z); occ.	0.1862(10), 0.5724(10); 0.072(1) Pd	0.231(10), 0.574(13); 0.07 Pd;
$U_{11}, U_{22}, U_{33}, U_{23}=U_{12}=0, U_{13};$	0.0147(4), 0.0174(4), 0.0137(4), 0.0051(3)	–
B_{iso}	–	0.76(11)
B1 in 8j (x,y,z); occ.; U_{iso}^c ;	0.3588(7), 0.1796(4), 0.1056(7); 1.0 B; 0.014(1)	^d 0.3588, 0.1796, 0.1056; 1.0 B;
B_{iso}	–	^d 1.0
B2 in 4i (x,0,z); occ.; U_{iso}	0.4019(10), 0.0913(11); 1.0 B; 0.019(2)	^d 0.4019, 0.0913; 1.0 B;
B_{iso}	–	^d 1.0
Residual electron density; max; min in (electrons/ nm^3) \times 1000	4.20; –2.89	–

^a Crystal structure data are standardized using the program Structure Tidy [42].

^b Anisotropic atomic displacement parameters U_{ij} in $[\text{10}^{-2} \text{nm}^2]$. The anisotropic temperature factor is defined as $\exp[-2\pi^2(U_{11}h^2\mathbf{a}^* + U_{22}k^2\mathbf{b}^* + U_{33}l^2\mathbf{c}^* + 2U_{23}kl\mathbf{b}^*\mathbf{c}^* + 2U_{12}hk\mathbf{a}^*\mathbf{b}^* + 2U_{13}hl\mathbf{a}^*\mathbf{c}^*)]$.

^c Isotropic atomic displacement parameters U_{iso} (B_{iso}) in $[\text{10}^{-2} \text{nm}^2]$. U_{iso} (B_{iso}) values were obtained via isotropic refinement procedure.

^d Fixed parameter.

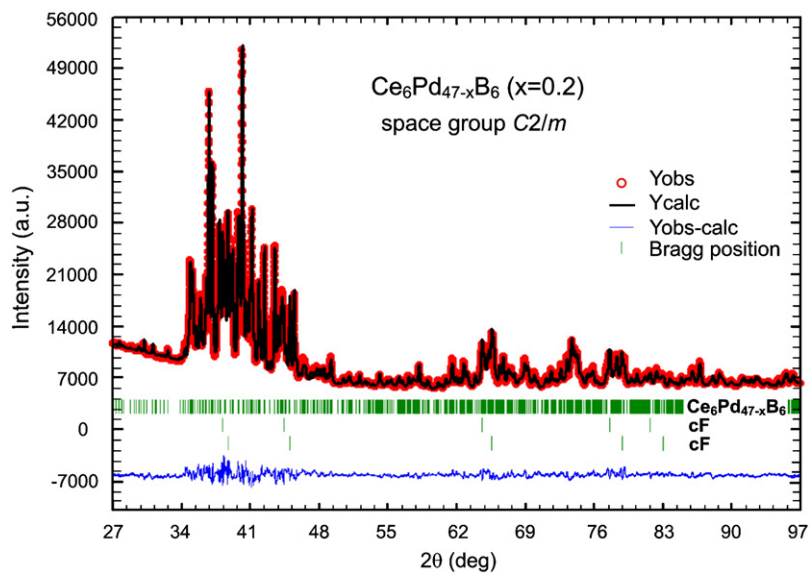


Fig. 1. X-ray diffraction pattern of $\text{Ce}_6\text{Pd}_{47-x}\text{B}_6$ ($x=0.2$). The solid line derives from the Rietveld refinement. $Y_{\text{obs}} - Y_{\text{calc}}$ is the intensity difference between experimental data and Rietveld calculations.

the fact that the monoclinic structure $\text{Ce}_3\text{Pd}_{25-x}\text{B}_{8-y}$ at higher boron contents does not form directly from the melt, a fact which made crystal growth difficult. Therefore single crystal structural studies were performed on specimens obtained from a congruently melting sample with about 25 at% B in the homologous system with La. The structure solution by direct methods in space group $P2_1/c$ revealed three atomic positions of La and 24 Pd sites; the atomic positions of boron atoms were found from difference Fourier synthesis. The structure refinement arrived at the arrangement of atomic sites and split positions (see Table 5) as typical for the structure $R_3\text{Pd}_{25-x}\text{B}_{8-y}$ ($R=\text{La}, \text{Ce}$) reported earlier [17]. The virtual increase of boron content in the chemical formula close to the boron-rich end of the homogeneity field as

compared to $\text{La}_3\text{Pd}_{25-x}\text{B}_{8-y}$ ($x=1.75, y=0.07$) essentially results from a significant reduction of the occupancy of Pd25 in site 2a (0,0,0) (from 71.2% Pd to 25.4% Pd) thus rendering the composition $\text{La}_3\text{Pd}_{25-x}\text{B}_{8-y}$ ($x=1.88; y=0.05$) at almost no variation of boron occupancy.

Transferring this structure model to Rietveld refinements of XPD data in the boron-rich end of the homogeneity field for $\text{Ce}_3\text{Pd}_{25-x}\text{B}_{8-y}$ allowed us to estimate the upper limit of boron incorporation in the isotypic Ce-phase (see Table 5 and Fig. 5).

Though a full-profile Rietveld refinement cannot distinguish between slight differences in the occupancies of palladium and boron atoms, the low residual values and minor differences between the observed and the calculated intensities for

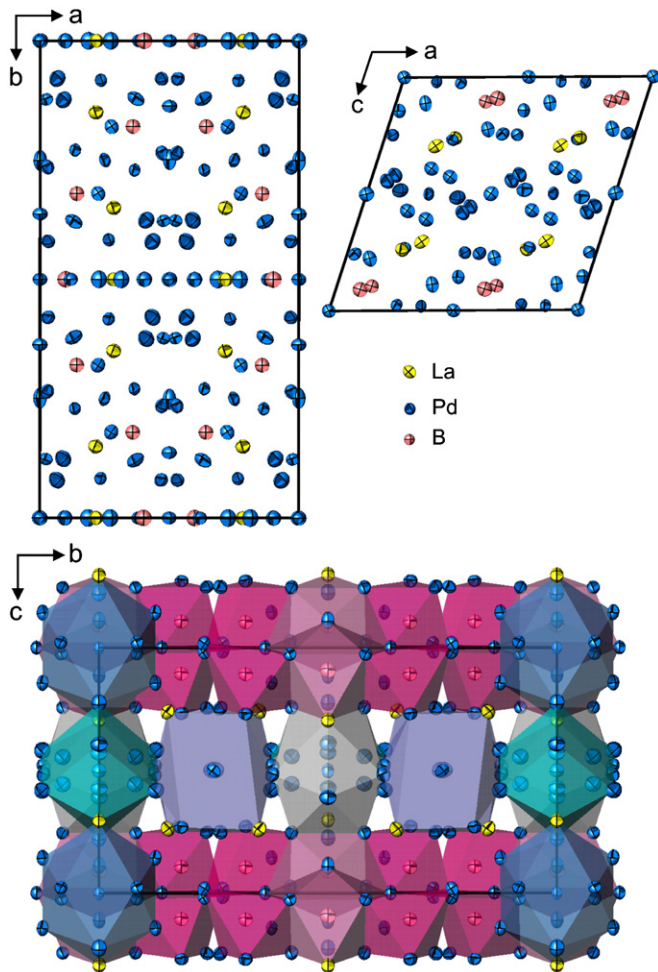


Fig. 2. $\text{La}_6\text{Pd}_{47-x}\text{B}_6$ ($x=0.19$) projected along crystallographic axes. Projection along [100] shows the packing of Pd-centered and B-centered polyhedra.

$\text{Ce}_3\text{Pd}_{25-x}\text{B}_{8-y}$ confirmed the structure model obtained from the La-crystal.

3.2.4. Phase equilibria at 850 °C

Phase analyses for selected samples are listed in Table 6 leading to the partial isothermal section at 850 °C as shown in Fig. 6. In agreement with literature data, the CePd_7 phase showed a rather large homogeneity region. Phase relations in the concentration field from 67 to 75 at% Pd are governed by formation of an extended solid solution CePd_3B_x and three monoclinic phases: τ_1 - $\text{Ce}_6\text{Pd}_{47-x}\text{B}_6$ (space group $C2/m$), τ_2 - $\text{CePd}_8\text{B}_{2-x}$ (space group $C2/c$) and τ_3 - $\text{Ce}_3\text{Pd}_{25-x}\text{B}_{8-y}$ (space group $P2_1/c$) [17]. The two later compounds coexist in equilibrium at 850 °C and form a homogeneity region extending from 14.5 to 23.8 at% B. Whilst the $C2/c$ monoclinic structure of the boron-poor end of the homogeneity field is stable in the whole temperature interval, the boron-rich structure with space group $P2_1/c$ is limited to lower temperatures. In as-cast condition the alloy $\text{Ce}_{9.5}\text{Pd}_{66.7}\text{B}_{23.8}$ showed the X-ray powder diffraction spectrum characteristic for the tetragonal $\text{Nd}_2\text{Pd}_{14+x}\text{B}_{5-x}$ type [16] but after annealing at 850 °C the low temperature phase ($P2_1/c$) was observed. Fig. 7 summarizes the phase relations among the phases $\text{CePd}_8\text{B}_{2-x}$, $\text{Ce}_3\text{Pd}_{25-x}\text{B}_{8-y}$ and $\text{Ce}_2\text{Pd}_{14+x}\text{B}_{5-y}$ in a $T-x$ diagram as a function of boron concentration. Lattice parameters as obtained from Rietveld refinements and single crystal X-ray data for the phases $\text{CePd}_8\text{B}_{2-x}$ and $\text{Ce}_3\text{Pd}_{25-x}\text{B}_{8-y}$ are shown in Fig. 8 as a function of the boron concentration x_B . For powder diffraction data, the content of boron was taken from the nominal composition thus explaining the small deviations from linearity for low boron contents. Although there is a smooth general trend of lattice parameters vs. x_B , the monoclinic angle shows a significant change manifesting a structural transition within the homogeneity field on rising boron contents as it was also inferred from Rietveld refinements and single crystal structural analyses. Starting from the boron-poor end, the increasing boron content (x) causes a slight increase of lattice parameters (Fig. 8).

Table 4

Single crystal structure data for $\text{CePd}_8\text{B}_{2-x}$.

Nominal composition	$\text{Ce}_{9.49}\text{Pd}_{75.93}\text{B}_{14.58}$	$\text{Ce}_{9.36}\text{Pd}_{74.91}\text{B}_{15.73}$
Space group	$C2/c$; no. 15	$C2/c$; no. 15
Structure type	$\text{CePd}_8\text{B}_{2-x}$	$\text{CePd}_8\text{B}_{2-x}$
Formula from refinement	$\text{CePd}_8\text{B}_{2-x}$ ($x=0.46$)	$\text{CePd}_8\text{B}_{2-x}$ ($x=0.32$)
Range for data collection	$2.36 < \theta < 36.27$	$2.36 < \theta < 36.23$
Crystal size	$45 \times 45 \times 35 \mu\text{m}^3$	$35 \times 35 \times 25 \mu\text{m}^3$
a (nm)	1.78104(4)	1.78277(4)
b (nm)	1.03723(3)	1.03626(3)
c (nm)	1.16314(3)	1.16172(3)
β (deg)	118.515(1)	118.541(1)
Reflections in refinement	3627 $F_o > 4\sigma(F_o)$ of 4348	3360 $F_o > 4\sigma(F_o)$ of 4435
Mosaicity	< 0.4	< 0.4
Number of variables	140	140
$R^2 = \sum F_o^2 - F_c^2 / \sum F_o^2$	0.0272	0.0359
R_{int}		
GOF	0.769	0.815
Extinction (Zachariasen)	0.00013(2)	0.00000(2)
Ce1 ^a in 8f (x, y, z); occ.	0.34719(2), 0.42582(4), 0.22263(3); 1.00 Ce	0.34694(3), 0.42580(4), 0.22265(4); 1.00 Ce
$U_{11}^b, U_{22}, U_{33}, U_{23}, U_{13}, U_{12}$	0.0103(2), 0.0106(2), 0.0109(2), -0.0001(1), 0.0049(1), 0.0002(1)	0.0096(2), 0.0103(2), 0.0103(2), -0.00012(14), 0.0046(1), 0.00013(13)
Ce2 in 4e ($0, y, 1/4$); occ.	0.37382(5); 1.00 Ce	0.37422(6); 1.00 Ce
$U_{11}, U_{22}, U_{33}, U_{23}=U_{12}=0, U_{13}$	0.0105(2), 0.0096(2), 0.0120(2), 0.0046(2)	0.0100(2), 0.0087(2), 0.0115(2), 0.0045(2)
Pd1 in 8f (x, y, z); occ.	0.07949(3), 0.24031(5), 0.52225(5); 1.00 Pd	0.07907(3), 0.24070(6), 0.52206(6); 1.00 Pd
$U_{11}, U_{22}, U_{33}, U_{23}, U_{13}, U_{12}$	0.0097(2), 0.0132(2), 0.0129(2), 0.0002(2), 0.0057(2), -0.0004(2)	0.0096(2), 0.0144(3), 0.0118(2), 0.0000(2), 0.0056(2), -0.0007(2)
Pd2 in 8f (x, y, z); occ.	0.09128(3), 0.19372(5), 0.14004(4); 1.00 Pd	0.09145(3), 0.19393(5), 0.14022(5); 1.00 Pd
$U_{11}, U_{22}, U_{33}, U_{23}, U_{13}, U_{12}$	0.0096(2), 0.0105(2), 0.0092(2), -0.0003(1), 0.0036(1), -0.0010(1)	0.0087(2), 0.0106(2), 0.0080(2), -0.0000(2), 0.0031(2), -0.0010(2)
Pd3 in 8f (x, y, z); occ.	0.16802(3), 0.00598(5), 0.04036(5); 1.00 Pd	0.16803(3), 0.00627(5), 0.04041(6); 1.00 Pd

Table 4 (continued)

$U_{11}, U_{22}, U_{33}, U_{23}, U_{13}, U_{12}$	0.0117(2), 0.0108(2), 0.0122(2), 0.0008(1), 0.0062(1), 0.0014(1)	0.0121(2), 0.0105(2), 0.0116(2), 0.0003(1), 0.0066(2), 0.0015(2)
Pd4 in 8f (x,y,z); occ.	0.17307(3), 0.20562(5), 0.39913(5); 1.00 Pd	0.17296(3), 0.20545(5), 0.39981(6); 1.00 Pd
$U_{11}, U_{22}, U_{33}, U_{23}, U_{13}, U_{12}$	0.0119(2), 0.0109(2), 0.0127(2), 0.00003(16), 0.0060(1), 0.0013(1)	0.0108(2), 0.0104(2), 0.0126(2), -0.00003(2), 0.0057(2), 0.0010(2)
Pd5 in 8f (x,y,z); occ.	0.17817(3), 0.41844(5), 0.24145(4); 1.00 Pd	0.17826(3), 0.41885(5), 0.24164(6); 1.00 Pd
$U_{11}, U_{22}, U_{33}, U_{23}, U_{13}, U_{12}$	0.0110(2), 0.0093(2), 0.0114(2), -0.0007(1), 0.0048(1), -0.0005(1)	0.0099(2), 0.0087(2), 0.0113(2), -0.0007(1), 0.0048(2), -0.0005(2)
Pd6 in 8f (x,y,z); occ.	0.18940(3), 0.27726(5), 0.03093(5); 1.00 Pd	0.18945(3), 0.27768(5), 0.03082(5); 1.00 Pd
$U_{11}, U_{22}, U_{33}, U_{23}, U_{13}, U_{12}$	0.0085(2), 0.0108(2), 0.0111(2), 0.0013(1), 0.0050(1), 0.0014(1)	0.0079(2), 0.0106(2), 0.0105(2), 0.0013(2), 0.0048(2), 0.0014(2)
Pd7 in 8f (x,y,z); occ.	0.26920(3), 0.16904(5), 0.27259(4); 1.00 Pd	0.26915(3), 0.16988(5), 0.27304(5); 1.00 Pd
$U_{11}, U_{22}, U_{33}, U_{23}, U_{13}, U_{12}$	0.0087(2), 0.0111(2), 0.0100(2), 0.0008(1), 0.0045(1), 0.0008(1)	0.0080(2), 0.0107(2), 0.0094(2), 0.0007(2), 0.0039(2), 0.0007(2)
Pd8 in 8f (x,y,z); occ.	0.31991(3), 0.04361(5), 0.51182(4); 1.00 Pd	0.31975(3), 0.04361(5), 0.51186(5); 1.00 Pd
$U_{11}, U_{22}, U_{33}, U_{23}, U_{13}, U_{12}$	0.0111(2), 0.0092(2), 0.0106(2), 0.0003(1), 0.0045(1), 0.0010(1)	0.0103(2), 0.0093(2), 0.0100(2), 0.0000(2), 0.0042(2), 0.0011(2)
Pd9 in 8f (x,y,z); occ.	0.41076(3), 0.13363(5), 0.23078(4); 1.00 Pd	0.41056(3), 0.13369(5), 0.23071(5); 1.00 Pd
$U_{11}, U_{22}, U_{33}, U_{23}, U_{13}, U_{12}$	0.0097(2), 0.0099(2), 0.0104(2), 0.0003(1), 0.0050(1), -0.00002(1)	0.0095(2), 0.0095(2), 0.0095(2), 0.0005(2), 0.0051(2), -0.0004(2)
Pd10 in 8f (x,y,z); occ.	0.45713(3), 0.09026(5), 0.02179(5); 1.00 Pd	0.45693(3), 0.08983(5), 0.02190(6); 1.00 Pd
$U_{11}, U_{22}, U_{33}, U_{23}, U_{13}, U_{12}$	0.0092(2), 0.0095(2), 0.0115(2), -0.0008(1), 0.0045(1), 0.0012(1)	0.0089(2), 0.0097(2), 0.0112(2), -0.0008(2), 0.0047(2), 0.0011(2)
Pd11 in 8f (x,y,z); occ.	0.46607(3), 0.32675(5), 0.12499(4); 1.00 Pd	0.46601(3), 0.32664(5), 0.12482(5); 1.00 Pd
$U_{11}, U_{22}, U_{33}, U_{23}, U_{13}, U_{12}$	0.0109(2), 0.0101(2), 0.0083(2), 0.0003(1), 0.0039(1), -0.0003(1)	0.0105(2), 0.0101(2), 0.0078(2), 0.0006(2), 0.0038(2), -0.0001(2)
Pd12 in 4e (0,y,1/4); occ.	0.07942(8); 0.995(3) Pd	0.07947(9); 1.007(4) Pd
$U_{11}, U_{22}, U_{33}, U_{23}=U_{12}=0, U_{13}$	0.0297(4), 0.0120(3), 0.0497(5), 0.0323(4)	0.0276(5), 0.0117(4), 0.0457(6), 0.0301(5)
Pd13 in 4a (0,0,0); occ.	1.00 Pd	1.00 Pd
$U_{11}, U_{22}, U_{33}, U_{23}, U_{13}, U_{12}$	0.0108(3), 0.0086(3), 0.0149(3), 0.0008(2), 0.0053(2), -0.0018(2)	0.0105(3), 0.0092(3), 0.0144(4), 0.0005(3), 0.0052(3), -0.0026(2)
B1 in 8f (x,y,z); occ.	0.2776(7), 0.113(1), 0.098(1); 1.00 B ^d	0.2785(8), 0.113(1), 0.097(1); 1.00 B ^d
U_{iso}^c	0.033(2)	0.032(2)
B2 in 8f (x,y,z); occ.	0.279(1), 0.313(2), 0.408(2); 0.31(2) B	0.274(1), 0.315(2), 0.409(2); 0.52(3) B
U_{iso}	0.004(3)	0.012(5)
B3 in 8f (x,y,z); occ.	0.3956(5), 0.0714(8), 0.4014(7); 1.00 B ^d	0.3958(6), 0.0711(9), 0.4002(9); 1.00 B ^d
U_{iso}	0.016(1)	0.017(2)
Residual electron density; max; min in (electrons/nm ³) × 1000	2.81; -2.09	4.13; -2.36

^a Crystal structure data are standardized using the program Structure Tidy [42].

^b Anisotropic atomic displacement parameters U_{ij} in [10² nm²]. The anisotropic temperature factor is defined as $\exp[-2\pi^2(U_{11}h^2a^{*2} + U_{22}k^2b^{*2} + U_{33}l^2c^{*2} + 2U_{23}khb^*c^* + 2U_{12}hka^*b^* + 2U_{13}hla^*c^*)]$.

^c Isotropic atomic displacement parameters U_{iso} in [10² nm²]. U_{iso} values were obtained via isotropic refinement procedure.

^d Fixed parameter.

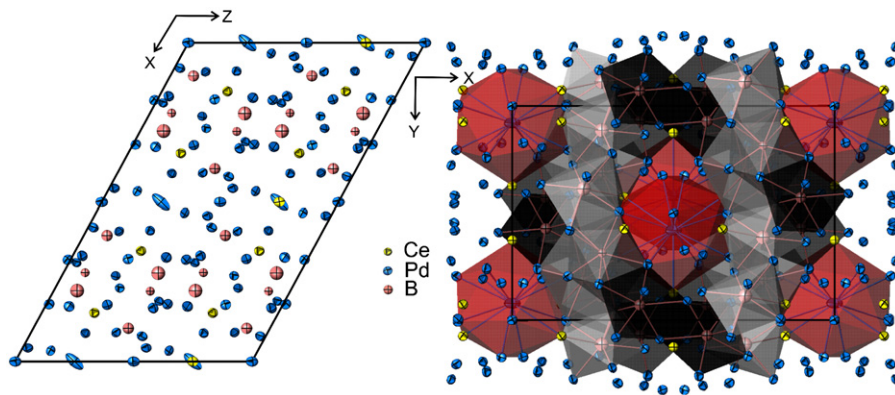


Fig. 3. CePd₈B_{2-x} structure projected along the monoclinic axis (left panel) and along z-axis (right panel). Coordination polyhedra of boron and Pd12 atoms are emphasized. The atoms are represented by their thermal ellipsoids.

This trend is consistent with the results of structural investigations for two different crystals of CePd₈B_{2-x} where the atomic positions of boron are occupied at 31(2)% and 52(3)% while the palladium content remains constant (Table 4). At about 18.3 at% of B, the formation of the Ce₃Pd_{25-x}B_{8-y}-type structure ($x=1.25$, $y=2.00$) was observed from X-ray single crystal data [17] revealing partially occupied atomic sites of palladium. With further increase

of boron content, the phase arrives at the boron-rich terminus of the homogeneity field with a continuous decrease of palladium occupancy at certain Pd-sites and a simultaneous enhancement of the occupancy in the boron sites (see Rietveld refinement for Ce₃Pd_{25-x}B_{8-y} ($x=1.87$; $y=0.05$) in Table 5).

Lattice constants for binary CePd₃ show the existence of a small homogeneity field and agree well with those reported in

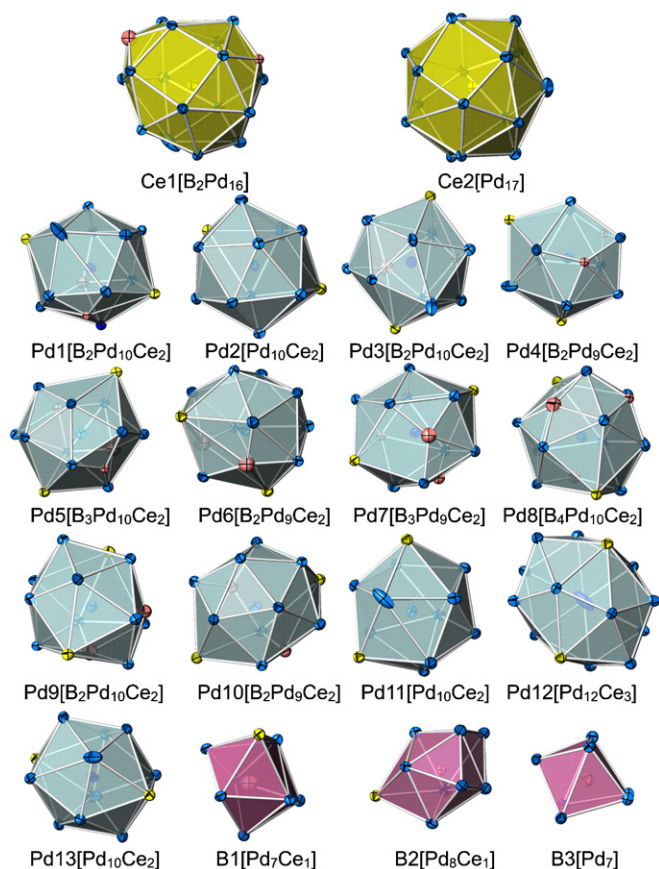


Fig. 4. Coordination polyhedra in the $\text{CePd}_8\text{B}_{2-x}$ structure.

literature: data after Thomson [12] (0.4129–0.4112 nm) compare well with our experiments for stoichiometric and Pd-rich compositions (0.41231(1)–0.41131(9) nm), respectively. Compositional dependences of lattice parameters for CePd_3B_x observed in our experiments (Fig. 9) revealed a significant expansion of the unit cell even for the alloy $\text{CePd}_3\text{B}_{0.125}$ saturating after reaching the maximum value $a=0.41954(5)$ nm at $\text{CePd}_3\text{B}_{0.25}$. Judging from phase analysis, single-phase alloys CePd_3B_x were found within the range $0 \leq x < 0.65$. Thus the limit of boron incorporation in CePd_3 was established at 13 at% in agreement with recent results [2]. Phase equilibria for concentrations < 66 at% Pd are dominated by CeB_4 and CeB_6 , which coexist with Pd_2B , Pd_5B_2 , $\text{Ce}_3\text{Pd}_{25-x}\text{B}_{8-y}$ and CePd_3B_x . The X-ray powder diffraction pattern observed for Ce_3Pd_5 does not agree with the spectrum calculated for the Th_3Pd_5 type [30]. The evaluation of the phase field $\text{CeB}_4 + \text{CePd}_3\text{B}_x + \text{Ce}_3\text{Pd}_5$ from lattice parameter variations has been guided not only by the non-stoichiometry of CePd_3B_x but by the existence of a certain homogeneity field for the CePd_3B_x binary as well.

3.3. Structural analysis

The X-ray single crystal and powder diffraction study revealed the existence of three different monoclinic structures in the palladium-rich corner of the Ce–Pd–B system. The phase $\text{CePd}_8\text{B}_{2-x}$ (for $x=0.46$ and 0.32) crystallizes in the space group $\text{C2}/c$ while for the remaining two phases the symmetry is reduced: for $\text{R}_3\text{Pd}_{25-x}\text{B}_{8-y}$ and $\text{La}_6\text{Pd}_{47-x}\text{B}_6$, respectively ($R=\text{La}, \text{Ce}$) the space groups $\text{P2}_1/c$ and $\text{C2}/m$ were established. All of them belong to the point group $2/m$. The space group $\text{P2}_1/c$ is a *klassengleiche subgroup* of index 2 of $\text{C2}/c$ and arises through the loss of Bravais translation symmetry. The formal group–subgroup

Table 5

Crystal structure data for the boron-rich members of the homogeneity field $\text{R}_3\text{Pd}_{25-x}\text{B}_{8-y}$ ($R=\text{La}, \text{Ce}$; space group $\text{P2}_1/c$ (no. 14); structure type $\text{La}_3\text{Pd}_{25-x}\text{B}_{8-y}$).

Nominal composition	$\text{La}_{8.8}\text{Pd}_{67.8}\text{B}_{23.4}$	$\text{Ce}_{8.8}\text{Pd}_{67.9}\text{B}_{23.3}$
Formula from refinement	$\text{La}_3\text{Pd}_{25-x}\text{B}_{8-y}$ ($x=1.88(1); y=0.05(1)$)	$\text{Ce}_3\text{Pd}_{25-x}\text{B}_{8-y}$ ($x=1.87; y=0.05$)
Range for data collection	$2.32 < \theta < 36.29$	$8^\circ < 2\theta < 100^\circ$
Diffractometer	Nonius KappaCCD, MoK α	Guinier–Huber image plate, CuK α_1
Crystal size	$45 \times 40 \times 40 \mu\text{m}^3$	–
a (nm)	1.17703(2)	1.17274(3)
b (nm)	1.05950(2)	1.05537(2)
c (nm)	1.60981(3)	1.60271(4)
β (deg)	102.121(1)	102.265(1)
Reflections in refinement	6886 $F_o > 4\sigma(F_o)$ of 9236	2351
Mosaicity	< 0.4	–
Number of variables	283	133
$R_F^2 = \sum F_o - F_c / \sum F_o^2$	0.0314	$R_F = \sum F_o - F_c / \sum F_o = 0.061$
GOF	1.019	$R_I = \sum I_o - I_c / \sum I_o = 0.056$
		$R_{\text{exp}} = [(\sum (N - P + C) / \sum w_i y_i^2)]^{1/2} = 1.61$
		$\chi^2 = (R_{\text{wp}}/R_e)^2 = 2.27$
R_{int}	–	–
Extinction (Zachariasen)	0.00013(1)	–
$R1^a$ in $4e(x, y, z)$; occ.	0.13407(3), 0.56656(4), 0.34960(3); 1.00 La	0.1465(9), 0.53(1), 0.3614(9); 1.00 Ce;
$U_{11}^b, U_{22}, U_{33}, U_{23}, U_{13}, U_{12}$	0.0088(1), 0.0099(2), 0.0105(1), –0.0008(1), 0.0018(1), 0.0000(1)	–
B_{iso}^c	–	0.9(3)
$R2$ in $4e(x, y, z)$; occ.	0.24378(3), 0.37245(3), 0.00087(2); 1.00 La	0.255(1), 0.378(1), 0.0008(12); 1.00 Ce;
$U_{11}, U_{22}, U_{33}, U_{23}, U_{13}, U_{12}$	0.0149(1), 0.0094(2), 0.0098(2), –0.002(1), 0.0024(1), 0.0005(1)	–
B_{iso}	–	0.7(3)
$R3$ in $4e(x, y, z)$; occ.	0.63199(3), 0.41179(4), 0.32954(3); 1.00 La	0.610(2), 0.410(1), 0.3265(9); 1.00 Ce;
$U_{11}, U_{22}, U_{33}, U_{23}, U_{13}, U_{12}$	0.0085(2), 0.0106(2), 0.0111(2), 0.0014(1), 0.0015(1), –0.0006(13)	–
B_{iso}	–	0.6(3)
$Pd1$ in $4e(x, y, z)$; occ.	0.00184(5), 0.34010(5), 0.23079(3); 1.00 Pd	0.014(1), 0.34(2), 0.234(1); 1.00 Pd;
$U_{11}, U_{22}, U_{33}, U_{23}, U_{13}, U_{12}$	0.0087(2), 0.0106(2), 0.0112(2), 0.0000(1), 0.0020(2), 0.0003(2)	–
B_{iso}	–	0.5(3)
$Pd2$ in $4e(x, y, z)$; occ.	0.03705(5), 0.31543(7), 0.41060(4); 1.00 Pd	0.038(1), 0.306(2), 0.407(1); 1.00 Pd;

Table 5 (continued)

$U_{11}, U_{22}, U_{33}, U_{23}, U_{13}, U_{12}$	0.0144(3), 0.0260(3), 0.0150(3), 0.0079(2), –0.0009(2), –0.0066(2)	–
B_{iso} Pd3 in 4e (x,y,z); occ. $U_{11}, U_{22}, U_{33}, U_{23}, U_{13}, U_{12}$	– 0.05200(5), 0.23530(5), 0.08706(3); 1.00 Pd 0.0104(2), 0.0134(2), 0.0105(2), 0.0011(2), 0.0020(2), 0.0020(2)	0.2(4) 0.060(1), 0.224(1), 0.082(1); 1.00 Pd; –
B_{iso} Pd4 in 4e (x,y,z); occ. $U_{11}, U_{22}, U_{33}, U_{23}, U_{13}, U_{12}$	– 0.05777(5), 0.08951(5), 0.32512(4); 1.00 Pd 0.0127(2), 0.0133(3), 0.0128(2), 0.0023(2), 0.0029(2), –0.0011(2)	0.6(4) 0.073(1), 0.099(2), 0.3194(9); 1.00 Pd; –
B_{iso} Pd5 in 4e (x,y,z); occ. $U_{11}, U_{22}, U_{33}, U_{23}, U_{13}, U_{12}$	– 0.06232(5), 0.59425(5), 0.04081(3); 1.00 Pd 0.0107(2), 0.0095(2), 0.0085(2), –0.0008(2), 0.0017(2), –0.0016(2)	0.9(4) 0.065(1), 0.584(1), 0.049(1); 1.00 Pd; –
B_{iso} Pd6 in 4e (x,y,z); occ. $U_{11}, U_{22}, U_{33}, U_{23}, U_{13}, U_{12}$	– 0.12404(5), 0.50086(5), 0.67403(4); 1.00 Pd 0.0098(2), 0.0102(2), 0.0142(2), –0.0020(2), 0.0033(2), –0.0004(2)	0.5(3) 0.142(2), 0.515(1), 0.6853(9); 1.00 Pd; –
B_{iso} Pd7 in 4e (x,y,z); occ. $U_{11}, U_{22}, U_{33}, U_{23}, U_{13}, U_{12}$	– 0.16269(4), 0.72456(5), 0.19062(3); 1.00 Pd 0.0086(2), 0.0094(2), 0.0087(2), –0.0007(2), 0.0008(2), 0.0009(2)	0.3(1) 0.179(1), 0.719(1), 0.188(1); 1.00 Pd; –
B_{iso} Pd8 in 4e (x,y,z); occ. $U_{11}, U_{22}, U_{33}, U_{23}, U_{13}, U_{12}$	– 0.17258(5), 0.82438(6), 0.02799(4); 1.00 Pd 0.0145(2), 0.0134(2), 0.0113(2), –0.0000(1), 0.0023(2), –0.0040(2)	0.3(2) 0.181(1), 0.824(2), 0.0363(9); 1.00 Pd; –
B_{iso} Pd9 in 4e (x,y,z); occ. $U_{11}, U_{22}, U_{33}, U_{23}, U_{13}, U_{12}$	– 0.19167(5), 0.45620(5), 0.17826(3); 1.00 Pd 0.0118(2), 0.0093(2), 0.0109(2), 0.0001(2), 0.0025(2), –0.0000(2)	0.8(3) 0.183(1), 0.450(1), 0.193(1); 1.00 Pd; –
B_{iso} Pd11 in 4e (x,y,z); occ. $U_{11}, U_{22}, U_{33}, U_{23}, U_{13}, U_{12}$	– 0.22375(5), 0.28997(5), 0.33113(4); 1.00 Pd 0.0096(2), 0.0103(2), 0.0132(2), 0.0017(2), 0.0019(2), –0.0003(2)	0.6(2) 0.225(1), 0.277(1), 0.332(1); 1.00 Pd; –
B_{iso} Pd12 in 4e (x,y,z); occ. $U_{11}, U_{22}, U_{33}, U_{23}, U_{13}, U_{12}$	– 0.27622(5), 0.20396(5), 0.18037(3); 1.00 Pd 0.0086(2), 0.0108(2), 0.0104(2), 0.0004(2), 0.0016(2), 0.0001(2)	0.4(3) 0.281(1), 0.193(2), 0.179(1); 1.00 Pd; –
B_{iso} Pd13 in 4e (x,y,z); occ. $U_{11}, U_{22}, U_{33}, U_{23}, U_{13}, U_{12}$	– 0.30923(5), 0.03496(5), 0.32618(3); 1.00 Pd 0.0117(2), 0.0092(2), 0.0105(2), 0.0008(2), 0.0022(2), 0.0003(2)	0.5(3) 0.309(2), 0.023(2), 0.337(1); 1.00 Pd; –
B_{iso} Pd14 in 4e (x,y,z); occ. $U_{11}, U_{22}, U_{33}, U_{23}, U_{13}, U_{12}$	– 0.32134(5), 0.62454(5), 0.09336(3); 1.00 Pd 0.0101(2), 0.0119(2), 0.0092(2), –0.0003(2), 0.0023(2), –0.0005(2)	0.6(2) 0.316(1), 0.627(2), 0.090(1); 1.00 Pd; –
B_{iso} Pd15 in 4e (x,y,z); occ. $U_{11}, U_{22}, U_{33}, U_{23}, U_{13}, U_{12}$	– 0.38115(5), 0.48399(5), 0.32659(3); 1.00 Pd 0.0104(2), 0.0088(2), 0.0110(2), 0.0005(2), 0.0032(2), 0.0005(2)	0.6(3) 0.391(1), 0.479(2), 0.330(1); 1.00 Pd; –
B_{iso} Pd16 in 4e (x,y,z); occ. $U_{11}, U_{22}, U_{33}, U_{23}, U_{13}, U_{12}$	– 0.43828(5), 0.17214(5), 0.07600(3); 1.00 Pd 0.0124(2), 0.0118(2), 0.0106(2), –0.0009(2), 0.0037(2), –0.0002(2)	0.5(2) 0.427(1), 0.164(2), 0.077(1); 1.00 Pd; –
B_{iso} Pd17 in 4e (x,y,z); occ. $U_{11}, U_{22}, U_{33}, U_{23}, U_{13}, U_{12}$	– 0.44012(5), 0.39728(5), 0.16865(5); 1.00 Pd 0.0131(2), 0.0104(2), 0.0101(2), –0.0000(2), 0.0032(2), –0.0018(2)	0.8(3) 0.445(2), 0.394(1), 0.1728(9); 1.00 Pd; –
B_{iso} Pd18 in 4e (x,y,z); occ. $U_{11}, U_{22}, U_{33}, U_{23}, U_{13}, U_{12}$	– 0.45269(5), 0.25380(5), 0.40857(3); 1.00 Pd 0.0118(2), 0.0092(2), 0.0087(2), 0.0007(2), 0.0017(2), 0.0007(2)	0.8(4) 0.449(1), 0.250(1), 0.400(1); 1.00 Pd; –
B_{iso} Pd19 in 4e (x,y,z); occ. $U_{11}, U_{22}, U_{33}, U_{23}, U_{13}, U_{12}$	– 0.50150(5), 0.14776(5), 0.26252(3); 1.00 Pd 0.0085(2), 0.0098(2), 0.0104(2), –0.0010(2), 0.0014(2), 0.0003(2)	0.6(2) 0.503(1), 0.149(2), 0.267(1); 1.00 Pd; –
B_{iso} Pd20 in 4e (x,y,z); occ. $U_{11}, U_{22}, U_{33}, U_{23}, U_{13}, U_{12}$	– 0.56102(5), 0.40071(5), 0.03421(3); 1.00 Pd 0.0107(2), 0.0100(2), 0.0075(2), –0.0000(2), 0.0011(2), 0.0010(2)	0.5(2) 0.562(1), 0.396(2), 0.035(1); 1.00 Pd; –
B_{iso} Pd21 in 4e (x,y,z); occ. $U_{11}, U_{22}, U_{33}, U_{23}, U_{13}, U_{12}$	– 0.66045(5), 0.25105(5), 0.16717(3); 1.00 Pd 0.0094(2), 0.0100(2), 0.0110(2), 0.0027(2), 0.0007(2), –0.0006(2)	0.7(3) 0.655(2), 0.253(2), 0.160(1); 1.00 Pd; –
B_{iso} Pd22 in 4e (x,y,z); occ. $U_{11}, U_{22}, U_{33}, U_{23}, U_{13}, U_{12}$	– 0.81994(5), 0.37102(5), 0.08933(5); 1.00 Pd 0.0101(2), 0.0114(2), 0.0095(2), 0.0001(2), 0.0026(2), –0.0006(2)	0.8(3) 0.822(1), 0.357(2), 0.089(1); 1.00 Pd; –

Table 5 (continued)

B_{iso}	–	0.6(3)
Pd25 in 2a (0,0,0); occ.	0.254(3) Pd	0.26(1) Pd;
$U_{11}, U_{22}, U_{33}, U_{23}, U_{13}, U_{12}$	0.0094(2), 0.0100(2), 0.0110(2), 0.0027(2), 0.0007(2), –0.0006(2)	–
B_{iso}	–	0.7(4)
Pd10 in 4e (x,y,z); occ.	0.21812(5), 0.0821(1), 0.02624(5); 0.948(2) Pd	0.220(1), 0.079(1), 0.0247(9); 0.95(1) Pd;
$U_{11}, U_{22}, U_{33}, U_{23}, U_{13}, U_{12}$	0.0148(2), 0.0118(2), 0.0149(2), –0.0020(1), 0.0022(2), 0.0014(2)	–
B_{iso}	–	0.9(4)
Pd10a in 4e (x,y,z); occ.	0.2466(9), 0.0924(9), 0.0053(7); 0.051(1) Pd	0.239(10), 0.100(9), 0.007(8); 0.05(1) Pd;
$U_{11}, U_{22}, U_{33}, U_{23}, U_{13}, U_{12}$	0.0148(2), 0.0118(2), 0.0149(2), –0.0020(1), 0.0022(2), 0.0014(2)	–
B_{iso}	–	0.9(4)
Pd23 in 4e (x,y,z); occ.	0.60634(5), 0.0730(1), 0.00904(4); 0.947(3) Pd	0.607(1), 0.095(2), 0.003(1); 0.95(1) Pd;
$U_{11}, U_{22}, U_{33}, U_{23}, U_{13}, U_{12}$	0.0109(3), 0.0122(4), 0.0124(3), 0.0004(2), 0.0037(2), 0.0003(2)	–
B_{iso}	–	0.8(4)
Pd23a in 4e (x,y,z); occ.	0.638(1), 0.137(1), 0.0196(7); 0.053(3) Pd	0.635(8), 0.168(10), 0.017(6); 0.05(1) Pd;
$U_{11}, U_{22}, U_{33}, U_{23}, U_{13}, U_{12}$	0.012(5), 0.016(7), 0.010(4), 0.005(4), 0.008(4), 0.005(4)	–
B_{iso}	–	0.9(3)
B1 in 4e (x,y,z); occ.	0.0082(7), 0.4329(8), 0.0974(5); 1.00 B	0.067(9), 0.425(10), 0.101(6); 1.00 B;
$U_{\text{iso}}^c, (B_{\text{iso}}^d)$	0.011(1)	0.5
B2 in 4e (x,y,z); occ.	0.1166(7), 0.1872(8), 0.2220(5); 1.00 B	0.145(10), 0.200(9), 0.224(7); 1.00 B;
$U_{\text{iso}} (B_{\text{iso}})$	0.012(1)	0.5
B3 in 4e (x,y,z); occ.	0.3123(7), 0.6155(8), 0.2272(5); 1.00 B	0.292(10), 0.622(11), 0.208(7); 1.00 B;
$U_{\text{iso}} (B_{\text{iso}})$	0.012(1)	0.5
B4 in 4e (x,y,z); occ.	0.3434(9), 0.3884(9), 0.4524(6); 1.00 B	0.366(8), 0.405(10), 0.455(6); 1.00 B;
$U_{\text{iso}} (B_{\text{iso}})$	0.020(2)	0.5
B5 in 4e (x,y,z); occ.,	0.3847(7), 0.2998(8), 0.2760(5); 1.00 B	0.403(9), 0.313(9), 0.303(6); 1.00 B;
$U_{\text{iso}} (B_{\text{iso}})$	0.013(1)	0.5
B6 in 4e (x,y,z); occ.	0.4942(7), 0.0533(8), 0.3951(5); 1.00 B	0.498(9), 0.016(9), 0.412(8); 1.00 B;
$U_{\text{iso}} (B_{\text{iso}})$	0.013(1)	0.5
B7 in 4e (x,y,z); occ.	0.8115(7), 0.3734(8), 0.2192(5); 1.00 B	0.803(10), 0.394(11), 0.216(4); 1.00 B;
$U_{\text{iso}} (B_{\text{iso}})$	0.010(1)	0.5
B8 in 4e (x,y,z); occ. ^d	0.6832(9), 0.2526(9), 0.0215(7); 0.947(3)	0.683(8), 0.234(9), 0.013(6); 0.95 B;
$U_{\text{iso}} (B_{\text{iso}})$	0.020(1)	0.5
Residual density; max; min in (electrons/nm ³) × 1000	4.401; –3.095	–

^a Crystal structure data are standardized using the program Structure Tidy [42].

^b Anisotropic atomic displacement parameters U_{ij} in [10² nm²]. The anisotropic temperature factor is defined as $\exp[-2\pi^2(U_{11}h^2a^{*2} + U_{22}k^2b^{*2} + U_{33}l^2c^{*2} + 2U_{23}khb^{*}c^{*} + 2U_{12}hka^{*}b^{*} + 2U_{13}hla^{*}c^{*})]$.

^c Isotropic atomic displacement parameters $U_{\text{iso}} (B_{\text{iso}})$ in [10² nm²]. $U_{\text{iso}} (B_{\text{iso}})$ values were obtained via isotropic refinement procedure.

^d Fixed parameter.

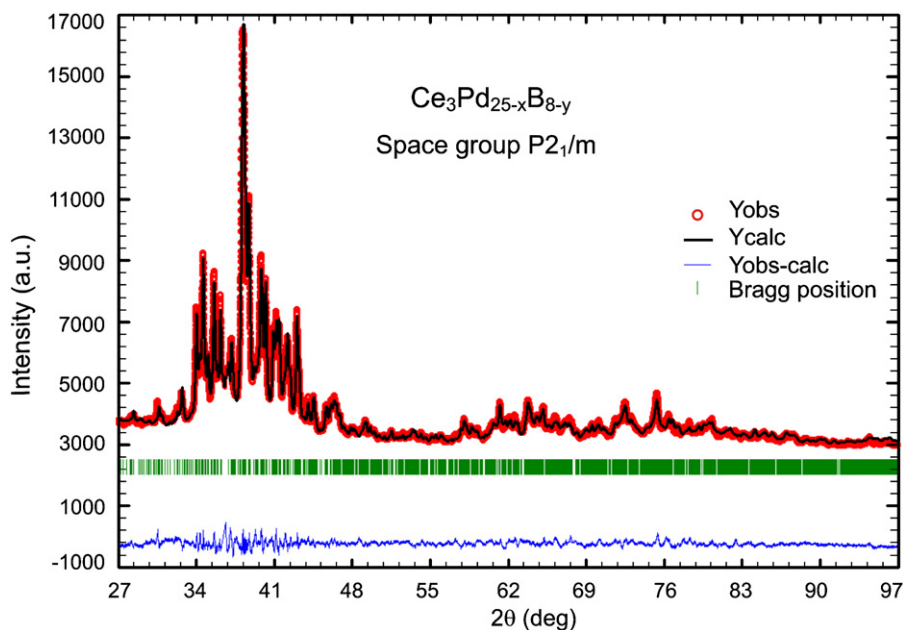


Fig. 5. X-ray diffraction pattern of $\text{Ce}_3\text{Pd}_{25-x}\text{B}_{8-y}$. The solid line derives from the Rietveld refinement. $Y_{\text{obs}} - Y_{\text{calc}}$ is the intensity difference between experimental data and Rietveld calculations.

Table 6
Crystallographic data of selected Ce–Pd–B alloys annealed at 850 °C.

No.	Nominal composition Ce–Pd–B (at%)	X-ray phase analysis	Space group	Structure type	Lattice parameters in nm		
					<i>a</i>	<i>b</i>	<i>c</i>
1	37.5–62.5	Ce ₃ Pd ₅		Unknown			
2	32–36–32	Ce ₃ Pd ₄	$R\bar{3}$	Pu ₃ Pd ₄	1.3722(2)		0.5812(1)
		CeB ₄	$P4/mbm$	UB ₄	0.72043(6)		0.40962(5)
		Ce ₃ Pd ₅		Unknown	–		–
4	28–28–44	CeB ₄	$P4/mbm$	UB ₄	0.72036(1)		0.40905(1)
		Ce ₃ Pd ₅		Unknown	–	–	–
5	27–70–3	CePd ₃ B _x	$Pm\bar{3}m$	CaTiO ₃	0.4181(2)		
		Ce ₃ Pd ₅		unknown	–		–
6	26–42–32	CePd ₃ B _x	$Pm\bar{3}m$	CaTiO ₃	0.41810(5)		–
		CeB ₄	$P4/mbm$	UB ₄	0.72066(6)		0.40973(5)
		Ce ₃ Pd ₅		Unknown	–		–
9	24.3–72.7–3.0	CePd ₃ B _x	$Pm\bar{3}m$	CaTiO ₃	0.41694(4)		
10	23.8–76.2	CePd ₃	$Pm\bar{3}m$	AuCu ₃	0.41231(1)		
11	23.5–70.6–5.9	CePd ₃ B _x	$Pm\bar{3}m$	CaTiO ₃	0.41954(5)		
12	22.2–66.6–11.1	CePd ₃ B _x	$Pm\bar{3}m$	CaTiO ₃	0.41954(3)		
13	22–55–23	CePd ₃ B _x	$Pm\bar{3}m$	CaTiO ₃	0.420(2)		
		CeB ₄ (traces)	$P4/mbm$	UB ₄	0.72053(8)		0.40952(8)
15	21.5–64.5–14.0	CePd ₃ B _x	$Pm\bar{3}m$	CaTiO ₃	0.4196(1)		–
		CeB ₆ (traces)	$Pm\bar{3}m$	CaB ₆	–		–
17	20–80	CePd ₃ cubic	$Pm\bar{3}m$	AuCu ₃	0.41131(9)		
					0.40623(8)		
19	20–60–20	CePd ₃ B _x	$Pm\bar{3}m$	CaTiO ₃	0.41951(5)		
		Ce ₃ Pd _{25–x} B _{8–y} (traces)	$C2/c$	La ₃ Pd _{25–x} B _{8–y}	–		–
		CeB ₆ (traces)	$Pm\bar{3}m$	CaB ₆	–		–
20	19–74–7	CePd ₃ B _x	$Pm\bar{3}m$	CaTiO ₃	0.4164(1)		
		Ce ₃ Pd _{25–x} B _{8–y} (traces)	$C2/c$	La ₃ Pd _{25–x} B _{8–y}	1.7822(3)	1.0389(1) $\beta=101.50(1)^\circ$	1.1678(1)
23	18–72–10	CePd ₃ B _x	$Pm\bar{3}m$	CaTiO ₃	0.41838(5)		
		Ce ₃ Pd _{25–x} B _{8–y}	$P2_1/c$	La ₃ Pd _{25–x} B _{8–y}	1.1722(1)	1.04535(9) $\beta=101.90(1)^\circ$	1.5989(1)
24	18–70–12	CePd ₃ B _x	$Pm\bar{3}m$	CaTiO ₃	0.41786(8)		
		Ce ₃ Pd _{25–x} B _{8–y}	$P2_1/c$	La ₃ Pd _{25–x} B _{8–y}	1.1737(1)	1.04439(8) $\beta=101.96(1)^\circ$	1.5955(2)
25	16.7–16.7–66.7	CePd ₃ B _x	$Pm\bar{3}m$	CaTiO ₃	0.41856(3)		
		CeB ₆	$Pm\bar{3}m$	CaB ₆	0.41410(1)		
		CeB ₄	$P4/mbm$	UB ₄	0.7209(2)		0.4094(2)
26	16–80–4	cubic	–	–	0.40629(8)		
27	16–78–6	cubic	–	–	0.4059(2)		
		cubic	–	–	0.40843(4) ^b		
28	15–50–35	CePd ₃ B _x	$Pm\bar{3}m$	CaTiO ₃	0.41961(5)		
		Ce ₃ Pd _{25–x} B _{8–y}	$P2_1/c$	La ₃ Pd _{25–x} B _{8–y}	1.1734(3)	1.0543(1) $\beta=102.08(2)^\circ$	1.6003(5)
		–	$Pm\bar{3}m$	–	–		–
		CeB ₆ (traces)		CaB ₆	–		–
30	14.3–71.4–14.3	CePd ₃ B _x	$Pm\bar{3}m$	CaTiO ₃	0.41782(3)		
		Ce ₃ Pd _{25–x} B _{8–y}	$P2_1/c$	La ₃ Pd _{25–x} B _{8–y}	1.17571(6)	1.04398(3) $\beta=102.07(1)^\circ$	1.59688(9)
32	13–77–10	Cubic	–	–	0.40842(3) ^{a,b}		
		CePd ₈ B _{2–x}	$C2/c$	CePd ₈ B _{2–x}	1.78112(7)	1.03634(3) $\beta=118.54(1)^\circ$	1.16195(4)

33	12–79–9	cubic CePd ₈ B _{2–x} (traces)	– C2/c	– CePd ₈ B _{2–x}	0.40567(9) –		
36	11–79.5–10.5	Ce ₆ Pd _{47–x} B ₆	C2/m	La ₆ Pd _{47–x} B ₆	1.03591(1)	1.80779(3) β = 108.32(1) [°]	1.01986(1)
37	11–78–11	cubic CePd ₈ B _{2–x}	C2/c	CePd ₈ B _{2–x}	0.40799(1) 0.40307(1) 1.7790(3)	1.0349(1) β = 118.75(1) [°] 1.80882(8) β = 108.33(1) [°]	1.1708(2) – 1.02065(5)
		Ce ₆ Pd _{47–x} B ₆	C2/m	La ₆ Pd _{47–x} B ₆	1.03647(5)		
40	10–80–10	cubic (traces) cubic CePd ₈ B _{2–x} (traces)	– C2/c	– CePd ₈ B _{2–x}	0.4085(1) 0.40483(1) ^a		
		Ce ₆ Pd _{47–x} B ₆ (traces) Ce ₆ Pd _{47–x} B ₆	C2/m C2/m	La ₆ Pd _{47–x} B ₆ La ₆ Pd _{47–x} B ₆	1.0375(1)	1.8058(2) β = 108.38(1) [°] 1.0379(1) β = 118.50(1) [°]	1.0216(1) 1.1641(2)
42	9.5–66.7–23.8	CePd ₈ B _{2–x} (traces)	C2/c	CePd ₈ B _{2–x}	1.7829(4)		
		cubic (traces) Ce ₃ Pd _{25–x} B _{8–y}	P2 ₁ /c	La ₃ Pd _{25–x} B _{8–y}	0.40343(4) 1.1747(1)	1.0567(1) β = 102.18(2) [°]	1.6045(1)
45	9.5–76.5–14	CePd ₈ B _{2–x}	C2/c	CePd ₈ B _{2–x}	1.7803(1)	1.03601(4) β = 118.55(1) [°]	1.16152(6)
		cubic Ce ₆ Pd _{47–x} B ₆ traces CePd ₈ B _{2–x}	C2/m C2/c	La ₆ Pd _{47–x} B ₆ CePd ₈ B _{2–x}	0.40471(9) ^a 1.7859(2)	1.0447(1) β = 118.54(1) [°]	1.1733(1)
47	9.2–74.2–16.6	CePd ₈ B _{2–x}	C2/c	CePd ₈ B _{2–x}	1.77691(2)	1.03904(1) β = 118.47(1) [°]	1.16875(2)
48	9.2–73.1–17.7	Ce ₃ Pd _{25–x} B _{8–y}	P2 ₁ /c	Ce ₃ Pd _{25–x} B _{8–y}	1.17332(4)	1.04300(2) β = 102.12(1)	1.59590(7)
49	9.2–80–10.8	cubic CePd ₈ B _{2–x}	C2/c	CePd ₈ B _{2–x}	0.40397(3) ^a 1.78136(9)	1.03657(3) β = 118.58(1) [°]	1.16492(5)
		Pd ₃ B (traces) Ce ₃ Pd _{25–x} B _{8–y}	Pnma P2 ₁ /c	Fe ₃ C La ₃ Pd _{25–x} B _{8–y}	1.1678(1)	1.04688(5) β = 102.06(1) [°]	1.5970(1)
52	9–45–46	CeB ₆ Pd ₅ B ₂	Pm $\bar{3}$ m C2/c	CaB ₆ Mn ₅ C ₂	0.41418(2) 1.2672(9)	0.4951(2) β = 96.9(1) [°]	0.5481(4)
		Ce ₃ Pd _{25–x} B _{8–y}	P2 ₁ /c	La ₃ Pd _{25–x} B _{8–y}	1.1745(2)	1.0542(1) β = 102.11(1) [°]	1.6023(3)
53	6.9–72.4–20.7	Pd ₃ B Ce ₃ Pd _{25–x} B _{8–y}	Pnma P2 ₁ /c	Fe ₃ C La ₃ Pd _{25–x} B _{8–y}	0.5458(2) 1.1734(4)	0.7563(3) 1.0455(2) β = 102.13(1) [°]	0.4847(2) 1.5966(5)
		Pd ₃ B CePd ₈ B _{2–x}	Pnma C2/c	Fe ₃ C CePd ₈ B _{2–x}	0.54619(5) 1.7799(2)	0.75700(7) 1.03883(7) β = 118.47(1) [°]	0.48471(5) 1.1672(3)
56	6–71–23	Pd ₃ B Ce ₃ Pd _{25–x} B _{8–y}	Pnma P2 ₁ /c	Fe ₃ C La ₃ Pd _{25–x} B _{8–y}	0.5455(1) 1.1630(3)	0.7558(2) 1.0313(2) β = 101.79(1) [°]	0.4841(1) 1.5861(4)
		cubic CePd ₈ B _{2–x} (traces)	C2/c	CePd ₈ B _{2–x}	0.40341(3) ^a 1.7807(1)	1.03827(4) β = 118.52(1) [°]	1.16764(6)
58	5–80–15	Pd ₃ B	Pnma	Fe ₃ C	0.54654(1)	0.7566(1)	0.4828(1)

^a Lattice constants evaluated according to a cubic subcell.

^b Lattice parameters determined from stress-annealed sample.

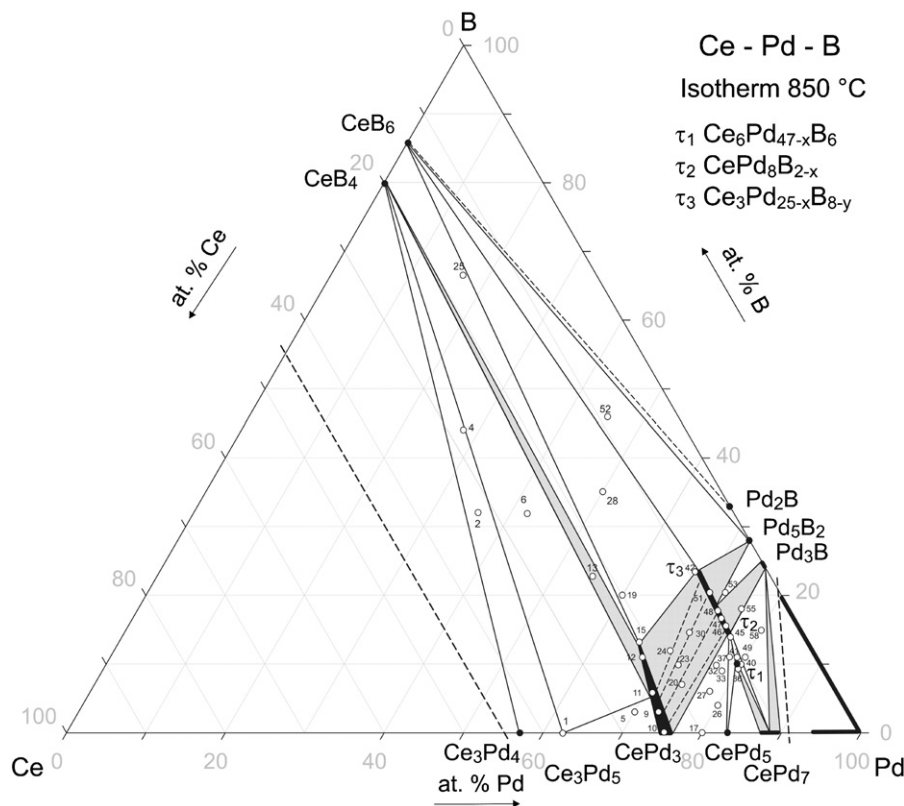


Fig. 6. System Ce–Pd–B; partial isothermal section at 850 °C up to 45 at% Ce. Some tie-lines are shown for the two-phase fields. Compositions and codes of the alloys prepared are shown as open circles (see also Table 8).

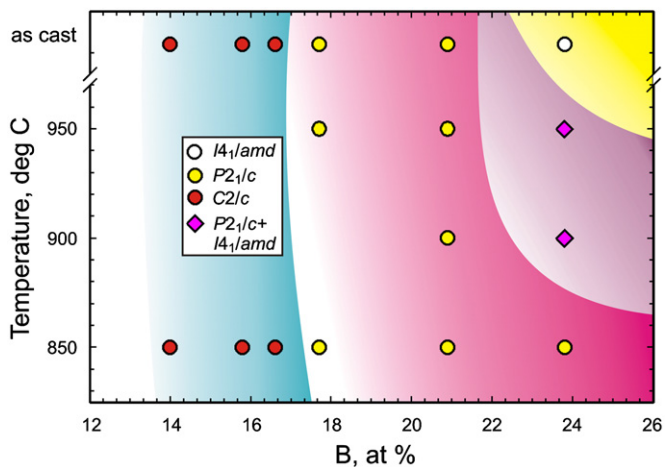


Fig. 7. $\text{CePd}_8\text{B}_{2-x}$, $\text{Ce}_3\text{Pd}_{25-x}\text{B}_{8-y}$ and $\text{Ce}_2\text{Pd}_{14+x}\text{B}_{5-y}$ structures vs. B concentration as a function of temperature.

relations for the structures $\text{CePd}_8\text{B}_{2-x}$, $\text{La}_3\text{Pd}_{25-x}\text{B}_{8-y}$ and $\text{Ce}_3\text{Pd}_{25-x}\text{B}_{8-y}$ are presented in Fig. 10 in Bärnighausen formalism [44]: the symmetry reduction is realized via a *klassengleiche* symmetry reduction $k2$ accompanied by shifts of origin $(0, 1/2, 1/2)$ and $(1/2, 1/2, 0)$ for both $\text{La}_3\text{Pd}_{25-x}\text{B}_{8-y}$ - and $\text{Ce}_3\text{Pd}_{25-x}\text{B}_{8-y}$ -structures, respectively, and a $(\mathbf{c}, \mathbf{b}, -\mathbf{a}-\mathbf{c})$ transformation of the unit cell. Fig. 2 (Supplementary Data) presents the geometrical relations in c direction between $\text{CePd}_8\text{B}_{2-x}$, $\text{Ce}_3\text{Pd}_{25-x}\text{B}_{8-y}$ and $\text{La}_3\text{Pd}_{25-x}\text{B}_{8-y}$. It can be seen that the presented structures differ essentially not only by significant shifts of atoms caused by increase of degree of freedom in the position of the atomic sites, but also by the

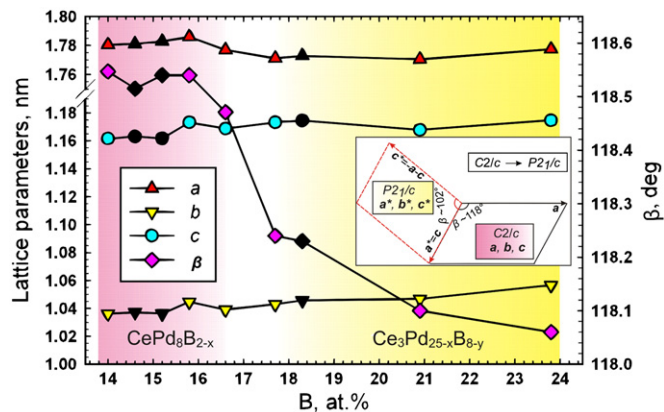


Fig. 8. Compositional dependence of lattice parameters for the phases $\text{CePd}_8\text{B}_{2-x}$ and $\text{Ce}_3\text{Pd}_{25-x}\text{B}_{8-y}$ from alloys quenched from 850 °C. Black symbols correspond to single crystal data. For better comparison, the $\text{Ce}_3\text{Pd}_{25-x}\text{B}_{8-y}$ lattice (space group $P2_1/c$) is used in the unit cell setting of the structure with space group $C2/c$. Geometrical relationships between two unit cell metrics and axial transformations are shown in the inset.

splitting of certain atomic positions which violate the $C2/c$ space group symmetry (Table 7).

All three structures are quite complex and, to facilitate the structural analysis, the approach of decomposition into characteristic structural units is helpful. In the present case, the most efficient technique was to express the structures in terms of simpler components located at certain planes. For simplification, only the Pd- and B-centered polyhedra are emphasized. In the crystal structures $\text{La}_3\text{Pd}_{25-x}\text{B}_{8-y}$ and $\text{CePd}_8\text{B}_{2-x}$, as seen along the long crystallographic axis (Fig. 11), infinite slabs centered at

$z \approx 1/4, 3/4$ and $x \approx 1/4, 3/4$, respectively, and composed of only boron-centered polyhedra alternate with slabs at $z \approx 0, 1/2$ (and $x \approx 0, 1/2$, respectively) containing also icosahedra centered by palladium. In $\text{CePd}_8\text{B}_{2-x}$, the palladium-centered icosahedra (Pd13 in 4a (0,0,0)) within the slabs at $x \approx 0, 1/2$ are connected at corners and form chains along the c -axis. In $\text{La}_3\text{Pd}_{25-x}\text{B}_{8-y}$, the palladium-centered icosahedra (Pd25 in 2a (0,0,0)) within the slabs at $z \approx 0, 1/2$ do not interconnect but are linked in b direction by B-centered edge-connected triangular prisms. Within the slabs with boron centered polyhedra, the coordination units of

boron are inter-linked in an irregular way in both structures (Fig. 11). The lower boron content in $\text{CePd}_8\text{B}_{2-x}$ as compared to the $\text{La}_3\text{Pd}_{25-x}\text{B}_{8-y}$ -structure can be visualized when the structures are viewed along the a - and c -direction, respectively: the slabs with boron-centered polyhedra in $\text{La}_3\text{Pd}_{25-x}\text{B}_{8-y}$ at $x \approx 1/2$ are replaced in $\text{CePd}_8\text{B}_{2-x}$ by slabs containing also polyhedra centered by palladium (compare Fig. 12b and d).

In the structure of $\text{La}_6\text{Pd}_{47-x}\text{B}_6$, the slabs at $y \approx 1/4$ and $3/4$ (view along b , Fig. 11) contain the chains of palladium centered polyhedra (Pd14 in 4f (1/4, 1/4, 1/2)), which are stretched parallel to the a -axis, and zig-zag chains of boron-centered triangular prisms running in the same direction. At $y \approx 0$ and $1/2$, the slabs are composed of a stacking of palladium-centered cubes (Pd16 in 2c (0, 0, 1/2) and icosahedra (Pd15 in 2d (0, 1/2, 1/2), Pd17 in 2a (0, 0, 0)), and tetragonal antiprisms of boron. If viewed along c , the structure shows (slabs at $z \approx 1/2$) infinite sheets of palladium-centered icosahedra and cubes joined at common corners (Fig. 12). At $z \approx 0$, the trigonal prisms and tetragonal antiprisms centered by boron are inter-connected and form ovals, which surround the palladium centered icosahedra (Pd17).

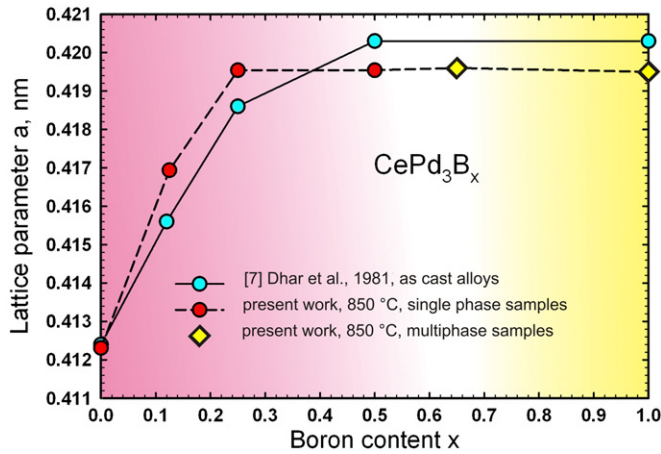


Fig. 9. Lattice parameter for CePd_3B_x vs. boron content.

3.4. The system Yb–Pd–B

3.4.1. Phase equilibria in the Yb–Pd–B system at 850 °C

Results obtained from the phase analysis of the samples are listed in Table 8 and the corresponding partial isothermal section at 850 °C is shown in Fig. 13. Judging from unit cell constant variations of YbPd_3B_x , the limit of B solubility in YbPd_3 corresponds to the value reported recently in the literature [15].

C12/c1		Ce1:8f	Ce1:4e	Pd1:8f	Pd2:8f	Pd3:8f	Pd4:8f	Pd5:8f	Pd6:8f	Pd7:8f	Pd8:8f	Pd9:8f	Pd10:8f	Pd11:8f	Pd12:4e	Pd13:4a	B1:8f	B2:8f ^{a)}	B3:8f	□:8f	□:8f	
$\text{CePd}_8\text{B}_{2-x}$		1	1	1	1	1	1	1	1	1	1	1	1	1	2	1	1	1	1	1	1	
 k2 c,b,-a-c shift of origin (1/2 1/2 0)		x	0	x	x	x	x	x	x	x	x	x	x	x	0	0	x	x	x	x	x	
 P12 ₁ /c1		Ce1:4e	Ce2:4e	Pd3:4e	Pd2:4e	Pd6:4e	Pd7:4e	Pd4:4e	Pd11:4e	Pd1:4e	Pd9:4e	Pd14:4e	Pd5:4e	Pd8:4e	□:4e	Pd25:2a ^{a)}	Pd28:2b ^{a)}	B3:4e	B2:4e	B1:4e	Pd10:4e ^{a)}	Pd26:4e ^{a)}
$\text{Ce}_3\text{Pd}_{25-x}\text{B}_{8-y}$		1	1	1	1	1	1	1	1	1	1	1	1	1	1	1	1	1	1	1	1	
x		x	x	x	x	x	x	x	x	x	x	x	x	x	0	1/2	x	x	x	x	x	
y		y	y	y	y	y	y	y	y	y	y	y	y	y	0	0	y	y	y	y	y	
z		z	z	z	z	z	z	z	z	z	z	z	z	z	0	0	z	z	z	z	z	

C12/c1		Ce1:8f	Ce1:4e	Pd1:8f	Pd2:8f	Pd3:8f	Pd4:8f	Pd5:8f	Pd6:8f	Pd7:8f	Pd8:8f	Pd9:8f	Pd10:8f	Pd11:8f	Pd12:4e	Pd13:4a	B1:8f	B2:8f	B3:8f	□:8f	□:8f	
$\text{CePd}_8\text{B}_{2-x}$		1	1	1	1	1	1	1	1	1	1	1	1	1	2	1	1	1	1	1	1	
 k2 c,b,-a-c shift of origin (0 1/2 1/2)		x	0	x	x	x	x	x	x	x	x	x	x	x	0	0	x	x	x	x	x	
 P12 ₁ /c1		La1:4e	La2:4e	Pd3:4e	Pd2:4e ^{a)}	Pd6:4e	Pd7:4e	Pd4:4e	Pd11:4e	Pd1:4e	Pd9:4e	Pd14:4e	Pd5:4e	Pd8:4e	□:4e	Pd25:2a ^{a)}	□:2b	B3:4e	B2:4e	B1:4e	Pd10:4e ^{a)}	Pd24:4e ^{a)}
$\text{La}_3\text{Pd}_{25-x}\text{B}_{8-y}$		1	1	1	1	1	1	1	1	1	1	1	1	1	1	1	1	1	1	1	1	
x		x	x	x	x	x	x	x	x	x	x	x	x	x	0	1/2	x	x	x	x	x	
y		y	y	y	y	y	y	y	y	y	y	y	y	y	0	0	y	y	y	y	y	
z		z	z	z	z	z	z	z	z	z	z	z	z	z	0	0	z	z	z	z	z	

Fig. 10. Group–subgroup scheme for $\text{CePd}_8\text{B}_{2-x}$, $\text{Ce}_3\text{Pd}_{25-x}\text{B}_{8-y}$ and $\text{La}_3\text{Pd}_{25-x}\text{B}_{8-y}$ structures. (a) Stays for partly occupied atomic position, empty squares correspond to unoccupied atomic sites.

Table 7
Structural parameters for the $\text{CePd}_8\text{B}_{2-x}$, $\text{Ce}_3\text{Pd}_{25-x}\text{B}_{8-y}$ [17] and $\text{La}_3\text{Pd}_{25-y}\text{B}_{8-y}$ [17].

$\text{CePd}_8\text{B}_{2-x}$ ($x=0.46$) in $\text{C2}/c$	$\text{Ce}_3\text{Pd}_{25-x}\text{B}_{8-y}$ ($x=1.25, y=2.00$) in $\text{P2}_1/c$	$\text{La}_3\text{Pd}_{25-y}\text{B}_{8-y}$ ($x=1.75, y=0.07$) in $\text{P2}_1/c$
Ce1 in 8f (x,y,z)	Ce1 (4e) 0.13011, 0.56995, 0.34940	La1 (4e) 0.13374, 0.56675, 0.34969
–	Ce3 (4e) 0.62792, 0.41846, 0.33996	La3 (4e) 0.63178, 0.41148, 0.33042
Ce2 in 4e (0,y,1/4)	Ce2 (4e) 0.24889, 0.37295, 0.00027	La2 (4e) 0.24480, 0.37282, 0.00077
Pd1 in 8f (x,y,z)	Pd3 (4e) 0.05574, 0.23852, 0.08312	Pd3 (4e) 0.05183, 0.23589, 0.08490
–	Pd18 (4e) 0.44672, 0.25726, 0.41328	Pd18 (4e) 0.45221, 0.25328, 0.40847
Pd2 in 8f (x,y,z)	Pd2 (4e) 0.04532, 0.30660, 0.40981	Pd2 (4e) 0.03801, 0.31167, 0.41038; Occ. 0.916
–	Pd16 (4e) 0.44466, 0.18241, 0.08311	Pd16 (4e) 0.43730, 0.17115, 0.07630
Pd3 in 8f (x,y,z)	Pd6 (4e) 0.12618, 0.50487, 0.67016	Pd6 (4e) 0.12355, 0.50450, 0.67239
–	Pd15 (4e) 0.37758, 0.49367, 0.33002	Pd15 (4e) 0.38022, 0.48256, 0.32652
Pd4 in 8f (x,y,z)	Pd7 (4e) 0.15969, 0.72332, 0.18952	Pd7 (4e) 0.16254, 0.72379, 0.19057
–	Pd12 (4e) 0.27867, 0.20492, 0.17735	Pd12 (4e) 0.27557, 0.20246, 0.18001
Pd5 in 8f (x,y,z)	Pd4 (4e) 0.06089, 0.08460, 0.32240	Pd4 (4e) 0.05714, 0.08773, 0.32382
–	Pd17 (4e) 0.43687, 0.40812, 0.17425	Pd17 (4e) 0.439428, 0.39686, 0.16881
Pd6 in 8f (x,y,z)	Pd11 (4e) 0.22249, 0.29117, 0.32778	Pd11 (4e) 0.22250, 0.28869, 0.33131
–	Pd21 (4e) 0.65775, 0.26336, 0.18023	Pd21 (4e) 0.66042, 0.25038, 0.16713
Pd7 in 8f (x,y,z)	Pd1 (4e) 0.00085, 0.33575, 0.22983	Pd1 (4e) 0.00199, 0.33761, 0.23095
–	Pd19 (4e) 0.50008, 0.15603, 0.26656	Pd19 (4e) 0.50137, 0.14704, 0.26224
Pd8 in 8f (x,y,z)	Pd9 (4e) 0.19173, 0.45523, 0.17910	Pd9 (4e) 0.19143, 0.45483, 0.17853
–	Pd13 (4e) 0.30976, 0.03844, 0.32335	Pd13 (4e) 0.30879, 0.03434, 0.32564
Pd9 in 8f (x,y,z)	Pd14 (4e) 0.31968, 0.63043, 0.08927	Pd14 (4e) 0.32107, 0.62460, 0.09332
–	Pd22 (4e) 0.81828, 0.36598, 0.08715	Pd22 (4e) 0.82049, 0.37011, 0.08916
Pd10 in 8f (x,y,z)	Pd5 (4e) 0.06414, 0.59214, 0.04177	Pd5 (4e) 0.06264, 0.59388, 0.04148
–	Pd20 (4e) 0.56123, 0.40224, 0.03899	Pd20 (4e) 0.56116, 0.40029, 0.03436
Pd11 in 8f (x,y,z)	Pd8 (4e) 0.16304, 0.82687, 0.03174	Pd8 (4e) 0.17168, 0.82557, 0.02820
Pd13 in 4a (0,0,0)	Pd25 (2a) 0,0,0; Occ. 0.50	Pd25 (2a) 0,0,0; Occ. 0.712
–	Pd28 (2b) 1/2,0,0; Occ. 0.50	–
Pd12 in 4e (0,y,1/4)	–	–
–	Pd10 (4e) 0.2255, 0.0826, 0.0166, Occ. 0.80	Pd10 (4e) 0.21592, 0.08348, 0.02277; Occ. 0.931
–	Pd27 (4e) 0.2700, 0.4187, 0.4868; Occ. 0.20	–
–	Pd26 (4e) 0.6543, 0.1594, 0.0283; Occ. 0.70	Pd24 (4e) 0.6381, 0.1306, 0.0192; Occ. 0.077
–	Pd23 (4e) 0.6055, 0.0746, 0.0116; Occ. 0.30	Pd23 (4e) 0.60608, 0.07331, 0.01000; Occ. 0.923
B3 in 8f (x,y,z)	B1 (4e) 0.0024, 0.4296, 0.1002	B1 (4e) 0.0088, 0.4315, 0.0987
–	B6 (4e) 0.4936, 0.0598, 0.3993	B6 (4e) 0.4938, 0.0525, 0.3947
B1 in 8f (x,y,z)	B3 (4e) 0.3130, 0.6147, 0.2208	B3 (4e) 0.3122, 0.6134, 0.2276
–	B7 (4e) 0.8125, 0.3740, 0.2183	B7 (4e) 0.8117, 0.3737, 0.2184
B2 in 8f (x,y,z); Occ. 0.31(2)	B2 (4e) 0.1249, 0.1858, 0.2222	B2 (4e) 0.1172, 0.1833, 0.2207
–	B5 (4e) 0.3761, 0.3059, 0.2824	B5 (4e) 0.3820, 0.3001, 0.2750
–	–	B4 (4e) 0.3395, 0.3877, 0.4522
–	–	B8 (4e) 0.6855, 0.2518, 0.0204; Occ. 0.923

The phase $\tau_1\text{-Yb}_2\text{Pd}_{13.6}\text{B}_5$ was found to form in single-phase conditions only in annealed alloys, whereas the X-ray powder diffraction pattern of as-cast samples yielded the spectra of YbPd_3B_x , Pd_5B_2 and YbB_6 indicating incongruent formation. Lattice parameters of the cubic phase from $\text{YbPd}_3\text{B}_x\text{-Pd}_3\text{B}$ equilibrium field fit well for the interval of values observed for $\text{YbPd}_3\text{-YbPd}_3\text{B}_x$ solubility range. Similarly to the Ce–Pd–B system, the X-ray powder diffraction data of stress-annealed samples containing higher contents of palladium beyond the $\text{YbPd}_3\text{-Pd}_3\text{B}$ tie-line yielded spectra which contained weak superstructure reflections but the base structure could be indexed according to a cubic unit cell with $a=0.405$ nm and cannot be regarded as belonging to any of the known binary boundary phases.

3.4.2. Crystal structure of $\tau_1\text{-Yb}_2\text{Pd}_{13.6}\text{B}_5$ and isotypic $\text{Lu}_2\text{Pd}_{13.2}\text{B}_5$

Due to the lack of good quality single crystals, Rietveld refinements were employed for the crystal structure investigation of $\tau_1\text{-Yb}_2\text{Pd}_{13.6}\text{B}_5$. The X-ray powder pattern of this compound suggested isotypism with the tetragonal structure of $\text{Sc}_4\text{Ni}_{29}\text{B}_{10}$ [45]. Recently three new $\text{Sc}_4\text{Ni}_{29}\text{B}_{10}$ -derivative structural arrangements have been reported, $\text{Nd}_2\text{Pd}_{14+x}\text{B}_{5-y}$ [16], ErNi_7B_3 [46] and $\text{Y}_2\text{Pd}_{14}\text{B}_5$ [47]. For this structural family, the boron atoms are found in structural units typical for rare earth intermetallic borides, namely trigonal prisms and tetragonal antiprisms (Fig. 14). Whilst the light rare earths, Gd and Th were found to favor the $\text{Nd}_2\text{Pd}_{14+x}\text{B}_{5-y}$ type of atomic arrangement with atomic position 8e partly occupied by palladium or boron atoms, Ni

containing borides with heavy rare earths ($R=\text{Tm, Lu}$) prefer the $\text{Sc}_4\text{Ni}_{29}\text{B}_{10}$ -type yielding Ni5 atom in a partly filled 4b special position and with boron in 8e [45]. In the $\text{Y}_2\text{Pd}_{14}\text{B}_5$ structure [47], the 4b atomic site is occupied by boron atoms whereas the 8e site remains unoccupied, thus leading to a shrinking of the unit cell in z direction as compared to other $\text{R}_2\text{Pd}_{14}\text{B}_5$ compounds (Fig. 15). Although full profile Rietveld analyses cannot differentiate between slight differences in the occupancies of B and Pd atoms, the small residual values for $\text{Yb}_2\text{Pd}_{13.6}\text{B}_5$ and $\text{Lu}_2\text{Pd}_{13.2}\text{B}_5$ based on the $\text{Y}_2\text{Pd}_{14}\text{B}_5$ structure inferred the isotypism of these compounds (Table 2).

3.5. Bonding and structural relationships

For all four structures, $\text{La}_6\text{Pd}_{47-x}\text{B}_6$, $\text{CePd}_8\text{B}_{2-x}$, $\text{La}_3\text{Pd}_{25-x}\text{B}_{8-y}$ and $\text{Yb}_2\text{Pd}_{14-x}\text{B}_5$, the nonstoichiometric nature arises from two types of disorder: (i) split of Pd sites, and (ii) partial occupancy of atom sites. Among them, the structures $\text{CePd}_8\text{B}_{2-x}$ and $\text{Yb}_2\text{Pd}_{14-x}\text{B}_5$ appear to be most ordered exhibiting only defects on one boron and one palladium site, respectively. The two remaining structures, $\text{La}_3\text{Pd}_{25-x}\text{B}_{8-y}$ and $\text{La}_6\text{Pd}_{47-x}\text{B}_6$, show in addition to partial occupancy of certain atom sites, the split of atomic positions of palladium. As it was shown above, the interatomic distances for completely occupied rare earth and palladium sites in all structures generally agree well with the sum of metal atom radii. Inspection of the atom environment of Pd11 and Pd13 in $\text{CePd}_8\text{B}_{2-x}$ revealed that the elevated ADP of

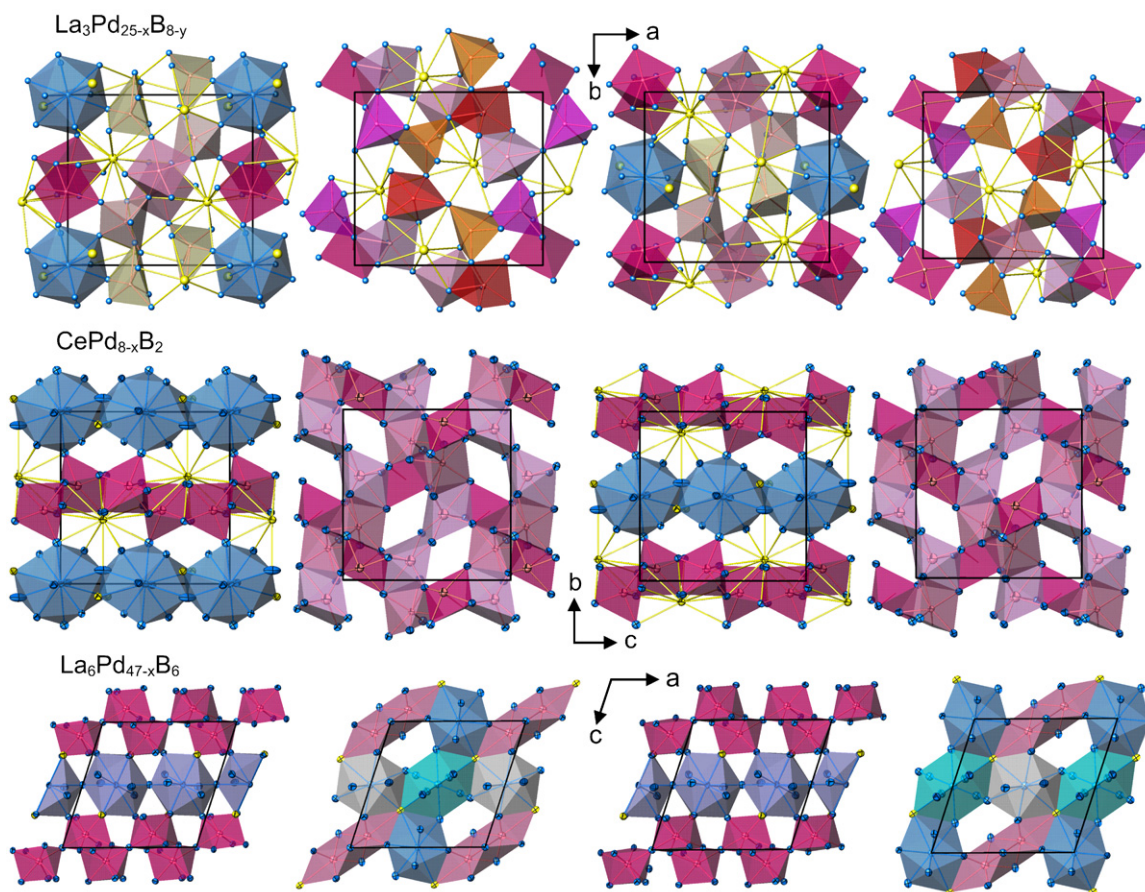


Fig. 11. Presentation of structures $\text{La}_3\text{Pd}_{25-x}\text{B}_{8-y}$, $\text{CePd}_{8-x}\text{B}_2$ and $\text{La}_6\text{Pd}_{47-x}\text{B}_6$ projected along the long crystallographic axis. Two-dimensionally infinite slabs are arranged in following order from left to right: for $\text{La}_3\text{Pd}_{25-x}\text{B}_{8-y}$ $z \approx 0, 1/4, 1/2, 3/4$; for $\text{CePd}_{8-x}\text{B}_2$ $x \approx 0, 1/4, 1/2, 3/4$; for $\text{La}_6\text{Pd}_{47-x}\text{B}_6$ $y \approx 1/4, 1/2, 3/4, 1$.

Pd12 within a distorted tri-capped hexagonal antiprism is a possible source of shortened bonds for the surrounding atoms ($d_{\text{Pd13-Pd11}} = 0.25588$ nm and $d_{\text{Pd13-Pd2}} = 0.26088$ nm). The shortening of Pd–B bonding is more evident: $d_{\text{B2-Pd4}} = 0.198$ nm and $d_{\text{B1-Pd3}} = 0.205$ nm in $\text{CePd}_8\text{B}_{2-x}$; $d_{\text{B2-Pd11}} = 0.2021$ nm and $d_{\text{B2-Pd8}} = 0.2084$ nm in $\text{La}_6\text{Pd}_{47-x}\text{B}_6$; $d_{\text{B5-Pd12}} = 0.2042$ nm and $d_{\text{B3-Pd7}} = 0.2086$ nm in $\text{La}_3\text{Pd}_{25-x}\text{B}_{8-y}$; however, this phenomenon appears to be a recurring feature also for binary borides with the Fe_3C -type structure being close in composition to our structures investigated: $d_{\text{B-Fe}} = 0.1981$ nm for Fe_3B , $d_{\text{B-Co}} = 0.1957$ nm for Co_3B and $d_{\text{B-Ni}} = 0.1966$ nm for Ni_3B . Besides Fe_3C type borides, the decrease of minimal distances was observed for certain borides rich in *d*-metal: $\text{Ho}_2\text{Ni}_{15}\text{B}_6$ ($d_{\text{B-Ni}} = 0.1891$ nm) [48], $\text{CeNi}_{12}\text{B}_6$ ($d_{\text{B-Ni}} = 0.198$ nm) [49], RNi_4B ($R = \text{Gd, Tb, Er}$; $d_{\text{B-Ni}} = 0.2045$ nm, 0.2046 nm and 0.2043 nm) [50] and $\text{Ce}_2\text{Co}_5\text{B}_2$ ($d_{\text{B-Co}} = 0.196$ nm) [51].

Although the structure types of $\text{La}_6\text{Pd}_{47-x}\text{B}_6$, $\text{CePd}_8\text{B}_{2-x}$, $\text{La}_3\text{Pd}_{25-x}\text{B}_{8-y}$ and $\text{Nd}_2\text{Pd}_{14+x}\text{B}_{5-y}$ are unique, relations to other structures can be easily recognized. Trigonal prisms connected by their vertical edges occur in *d*-metal rich borides, such as in the structure of CeCo_3B_2 and in the related structures of $\text{Nd}_2\text{Fe}_{14}\text{B}$ [52], $\text{Ce}_2\text{Ir}_5\text{B}_2$ [53], $\text{Ce}_2\text{Co}_5\text{B}_2$ [51], $\text{Ca}_3\text{Ni}_7\text{B}_2$ [54]. They differ from the title compounds by the way of stacking into larger structural fragments. In the structure of CeCo_3B_2 , six boron atoms are bonded to each cerium atom and the columns made of boron centered triangular prisms are stretched laterally along *c*-direction. In $\text{Ce}_2\text{Ir}_5\text{B}_2$, $\text{Ce}_2\text{Co}_5\text{B}_2$ and $\text{Ca}_3\text{Ni}_7\text{B}_2$, the fragments of CeCo_3B_2 are interleaved by structural fragments of Laves phases.

In $\text{La}_6\text{Pd}_{47-x}\text{B}_6$, there are two distinct atomic positions of boron. B2 atoms are found in the Archimedean antiprisms capped

on one rectangular side by one additional La2 atom. The antiprismatic coordination for boron is not so frequent in the structures of *d*-metal-rich ternary borides. Fragments formed by six Archimedean prisms linked via an empty cube were observed in the structure of τ -phases (Cr_{23}C_6 -type) [43]. Another example is the structure of $\text{Nd}_2\text{Pd}_{14+x}\text{B}_{5-y}$ where distorted squared antiprisms are inter-connected through a rectangular face [16]. Similarly, in the structure of $\text{La}_6\text{Pd}_{47-x}\text{B}_6$, the Archimedean antiprisms are also inter-connected via rectangular faces where the opposite rectangular faces are shared each with a polyhedron centered by La (see Fig. 16c).

B1 is surrounded by seven atoms of palladium: six atoms form the triangular prism and one additional atom is located against the rectangular face of the trigonal prism. Two mono-capped triangular prisms of B1 share a common edge. Three La atoms are bonded to B1: two La are linked with boron via two rectangular faces of the triangular prism and the additional La atom is bonded through the triangular face formed by an additional Pd-atom (Fig. 16a–b). Lanthanum atoms, involved in these blocks, interconnect via common faces and corners. If the structure is viewed along *a*, those slabs repeat at $x \approx 1/4$ and $3/4$. Similar fragments were observed in $\text{Nd}_2\text{Fe}_{14}\text{B}$ (Fig. 16d) where three rare earth atoms are bound to one boron atom through the rectangular faces of boron centered triangular prisms, and neodymium-centered polyhedra are inter-connected via common faces and corners. However the slabs formed in $\text{Nd}_2\text{Fe}_{14}\text{B}$ are relatively flat as compared to $\text{La}_6\text{Pd}_{47-x}\text{B}_6$, because the neodymium and boron atoms reside in the same planes (Nd in $4g(x, y, 0)$; Nd in $4f(x, x, 0)$; B in $4f(x, x, 0)$, whereas the atomic coordinate *x* for La and B in $\text{La}_6\text{Pd}_{47-x}\text{B}_6$ are different (La 1 in $8j(x, y, z)$ $x = 0.28483(3)$,

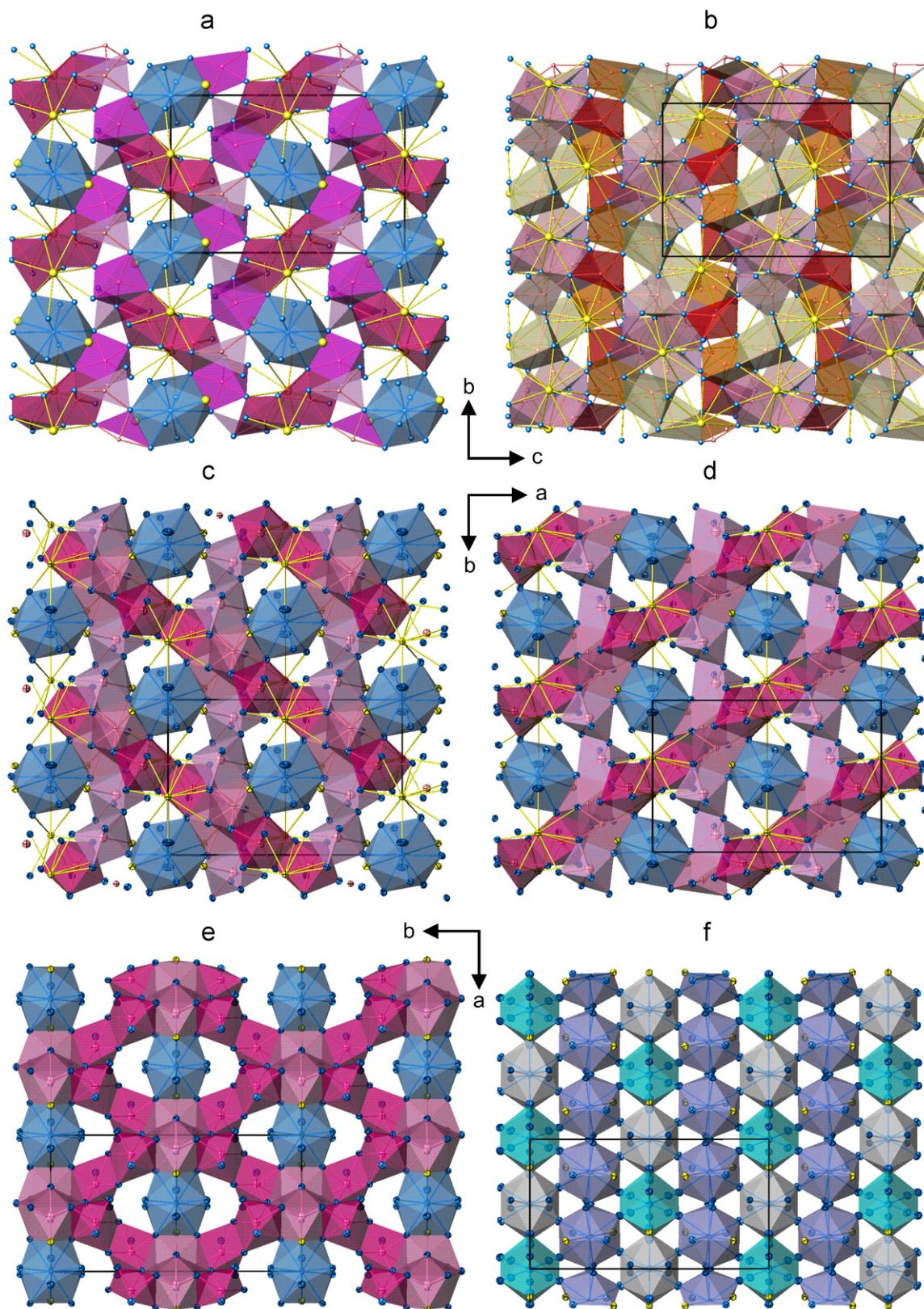


Fig. 12. Comparison of structures $\text{La}_3\text{Pd}_{25-x}\text{B}_{8-y}$, $\text{CePd}_8\text{B}_{2-x}$ and $\text{La}_6\text{Pd}_{47-x}\text{B}_6$ projected along [100], [001] and [010]. Slabs in $\text{La}_3\text{Pd}_{25-x}\text{B}_{8-y}$ at $x=0$, 1 (a), $x \approx 1/2$ (b); for $\text{CePd}_8\text{B}_{2-x}$ at $z=0$, 1 (c), $z \approx 1/2$ (d); for $\text{La}_6\text{Pd}_{47-x}\text{B}_6$ $z \approx 0$, 1 (e), $z \approx 1/2$ (f).

$y=0.35008(2)$, $z=0.26059(4)$; La2 in 4i ($x,0,z$) $x=0.21660(5)$, $z=0.29506(5)$; B1 in 8j (x,y,z) $x=0.3588(7)$, $y=0.1796(4)$, $z=0.1056(7)$.

As shown in Fig. 16e–k, the fragments observed in $\text{La}_6\text{Pd}_{47-x}\text{B}_6$ (e.g., edge sharing triangular prisms centered by boron atoms; squared antiprism as a coordination unit of boron; blocks of boron

Table 8

Crystallographic data of Yb–Pd–B alloys annealed at 850 °C.

No.	Nominal composition Yb–Pd–B (at%)	X-ray phase analysis	Space group	Structure type	Lattice parameters in nm		
					<i>a</i>	<i>b</i>	<i>c</i>
2	33.3–66.6	YbPd ₂					
3	30–62–8	YbPd ₃ B _x	<i>Pm</i> $\bar{3}$ <i>m</i>	CaTiO ₃	0.40713(4)		
6	25–75	YbPd ₂ (traces) CePd ₃	<i>Pm</i> $\bar{3}$ <i>m</i>	AuCu ₃	0.40499(1)		
7	24–50–26	YbPd ₃ B _x	<i>Pm</i> $\bar{3}$ <i>m</i>	CaTiO ₃	0.4083(1)		
		YbB ₂	<i>P6/mmm</i>	AlB ₂	0.32480(1)		0.37303(1)
		YbB ₄	<i>P4/mbm</i>	UB ₄	0.70574(3)		0.39902(2)
10	22–62–16	YbPd ₃ B _x	<i>Pm</i> $\bar{3}$ <i>m</i>	CaTiO ₃	0.40990(5)		
		YbB ₄ (traces)	<i>P4/mbm</i>	UB ₄			
11	20.8–79.2	YbPd ₃	<i>Pm</i> $\bar{3}$ <i>m</i>	AuCu ₃	0.40372(6)		
		Pd _{1–x} Yb _x	<i>Fm</i> $\bar{3}$ <i>m</i>	Pd	0.39510(8)		
12	20–60–20	YbPd ₃ B _x	<i>Pm</i> $\bar{3}$ <i>m</i>	CaTiO ₃	0.40860(4)		
		YbB ₆	<i>Pm</i> $\bar{3}$ <i>m</i>	CaB ₆	0.41345(6)		
		Yb ₂ Pd _{14–x} B ₅ (traces)	<i>I4₁/amd</i>	Y ₂ Pd ₁₄ B ₅ -related			
14	20–50–30	YbPd ₃ B _x	<i>Pm</i> $\bar{3}$ <i>m</i>	CaTiO ₃	0.40857(2)		
		YbB ₆	<i>Pm</i> $\bar{3}$ <i>m</i>	CaB ₆	0.4127(1)		
15	16.6–72.2–11.1	YbPd ₃ B _x	<i>Pm</i> $\bar{3}$ <i>m</i>	CaTiO ₃	0.40760(4)		
		Pd ₃ B	<i>Pnma</i>	Fe ₃ C	0.54610(3)	0.75612(4)	0.48491(4)
17	15–76–9	YbPd ₃ B _x	<i>Pm</i> $\bar{3}$ <i>m</i>	CaTiO ₃	0.40686(3)		
18	14–18–68	YbB ₆	<i>Pm</i> $\bar{3}$ <i>m</i>	CaB ₆	0.41478(1)		
		YbPd ₃ B _x (traces)	<i>Pm</i> $\bar{3}$ <i>m</i>	CaTiO ₃			
		Yb ₂ Pd _{14–x} B ₅	<i>I4₁/amd</i>	Y ₂ Pd ₁₄ B ₅ -related	0.83826(3)		1.6609(1)
19	11–79–10	Cubic			0.40512(2)		
		YbPd ₃	<i>Pm</i> $\bar{3}$ <i>m</i>	AuCu ₃	0.4036(5)		
21	9.5–66.7–23.8	Yb ₂ Pd _{14–x} B ₅	<i>I4₁/amd</i>	Y ₂ Pd ₁₄ B ₅ -related	0.83813(2)		1.66034(5)
		YbPd ₃ B _x	<i>Pm</i> $\bar{3}$ <i>m</i>	CaTiO ₃	0.40867(4)		
		Pd ₅ B ₂	<i>C2/c</i>	Mn ₅ C ₂	1.2802(1)	0.49739(4) $\beta=97.08(1)^\circ$	0.54094(7)
22	9.1–27.3–63.6	Yb ₂ Pd _{14–x} B ₅	<i>I4₁/amd</i>	Y ₂ Pd ₁₄ B ₅	0.83788(2)		1.6624(1)
		YbB ₆	<i>Pm</i> $\bar{3}$ <i>m</i>	CaB ₆	0.41472(3)		
		Pd ₅ B ₂	<i>C2/c</i>	Mn ₅ C ₂	1.2805(1)	0.49718(3) $\beta=97.16(1)^\circ$	0.54226(6)
23	6.9–72.4–20.7	YbPd ₃ B _x	<i>Pm</i> $\bar{3}$ <i>m</i>	CaTiO ₃	0.40803(6)		
		Pd ₅ B ₂	<i>C2/c</i>	Mn ₅ C ₂	1.2774(1)	0.49482(1)	0.54674(3)
		Pd ₃ B	<i>Pnma</i>	Fe ₃ C	0.5459(1)	$\beta=97.07(1)^\circ$ 0.7573(1)	0.4853(1)
24	6–38–54	YbB ₆	<i>Pm</i> $\bar{3}$ <i>m</i>	CaB ₆	0.41476(3)		
		Pd ₂ B	<i>Pnnm</i>	CaCl ₂	0.46949(2)	0.51238(2)	0.31071(1)
		YbB ₁₂ (traces)	<i>Fm</i> $\bar{3}$ <i>m</i>	UB ₁₂			
25	6–75–19	YbPd ₃ B _x	<i>Pm</i> $\bar{3}$ <i>m</i>	CaTiO ₃	0.4069(1)		
		Pd ₃ B	<i>Pnma</i>	Fe ₃ C	0.5462(1)	0.7561(2)	0.4852(1)
26	4–78–18	Cubic			0.40574(3)		
		Pd ₃ B	<i>Pnma</i>	Fe ₃ C	0.54764(1)	0.75593(1)	0.48578(1)

atom bonded to three rare earth atoms; face and corner connected polyhedra of rare earth atoms) are also present in the structures of CePd₈B_{2–x} and La₃Pd_{25–x}B_{8–y}. Although these three structures can be considered as a packing of structural fragments typical for Nd₂Fe₁₄B and Nd₂Pd_{14+x}B_{5–y}, the mutual dispositions of blocks are different.

In the following section, physical properties will be evaluated, particularly those of Yb₂Pd_{13.6}B₅ as a detailed description of the physical behavior of the Ce–Pd–borides will be the subject of an independent forthcoming article. Furthermore, we will use as a short notation Yb₂Pd₁₄B₅ instead of Yb₂Pd_{13.6}B₅.

3.6. Physical properties of τ_1 -Yb₂Pd_{13.6}B₅

To reveal the principal physics of Yb₂Pd₁₄B₅ the temperature dependent specific heat, temperature dependent electrical resistivity and magnetic measurements were performed. Lu₂Pd₁₄B₅ was taken as a non-magnetic analog.

The heat capacity data, $C_p(T)$, down to 2 K of Yb₂Pd₁₄B₅ and Lu₂Pd₁₄B₅ are presented in Fig. 17a. The lack of distinct anomalies in $C_p(T)$ for Lu₂Pd₁₄B₅ indicates the absence of structural transitions in the entire temperature range studied. Within the low temperature limit ($T < 5$ K) the heat capacity can be accounted for in terms of $C_p = \gamma T + \beta T^3$, yielding a Sommerfeld value $\gamma = 17$ mJ mol⁻¹ K⁻² and $\beta = 0.0019$ J mol⁻¹ K⁻⁴, revealing a Debye temperature $\theta_D^{LT} = 282$ K as typical for metal-rich borides.

In order to explore the vibrational properties of the lattice also at higher temperatures, the electronic contribution to the specific heat was subtracted and a model consisting of a combination of Debye and Einstein functions was adopted. Thermal expansion of the crystallographic unit cell, especially at high temperatures, was not taken in to account. Considering ~ 21 atoms per formula unit, the phonon dispersion relation of Yb₂Pd₁₄B₅ consists of three acoustic and 60 optical branches. The former constitutes the Debye contribution, while the latter form the Einstein part. A fit results in a Debye temperature $\theta_D = 88$ K and three Einstein

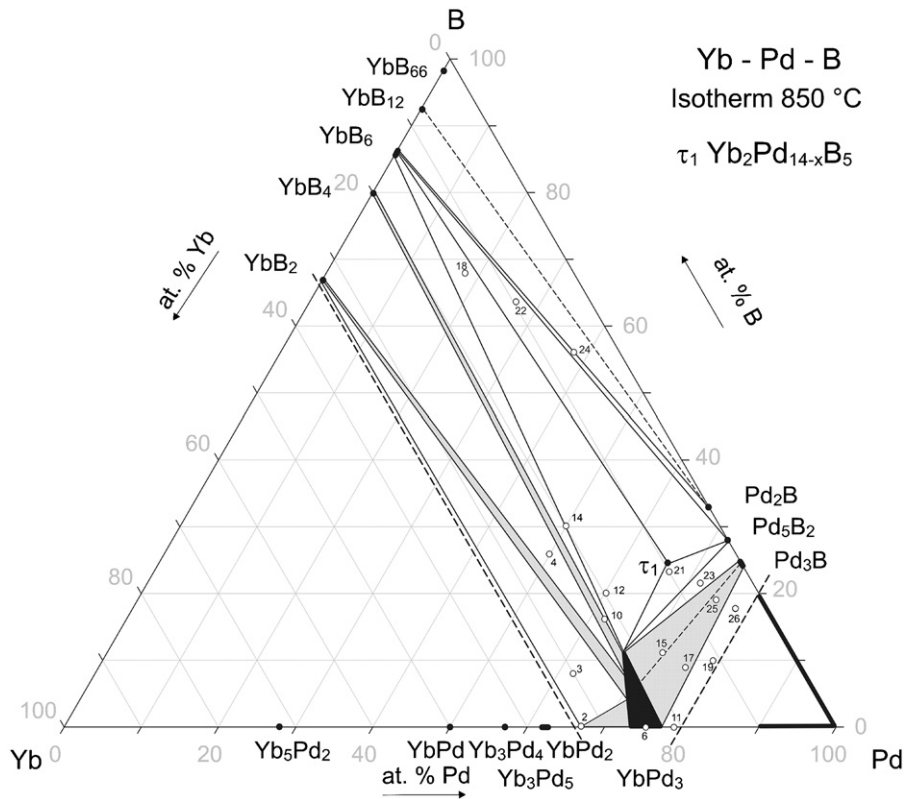


Fig. 13. System Yb-Pd-B; partial isothermal section at 850 °C up to 33 at% Yb. Alloys prepared are shown as empty circles (see also Table 8).

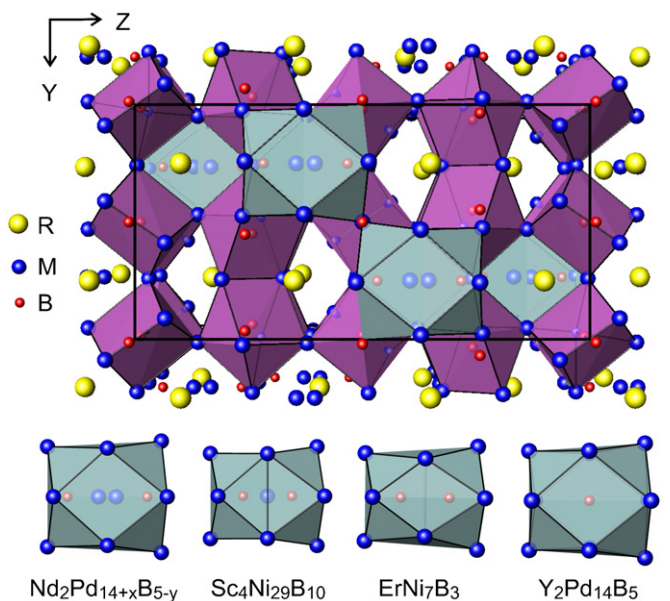


Fig. 14. Crystal structure of $\text{Yb}_2\text{Pd}_{14+x}\text{B}_{5-y}$ in three dimensional view along [100] axis and coordination polyhedra of $\text{Pd}_5(\text{B}_2)$ atoms in related structures.

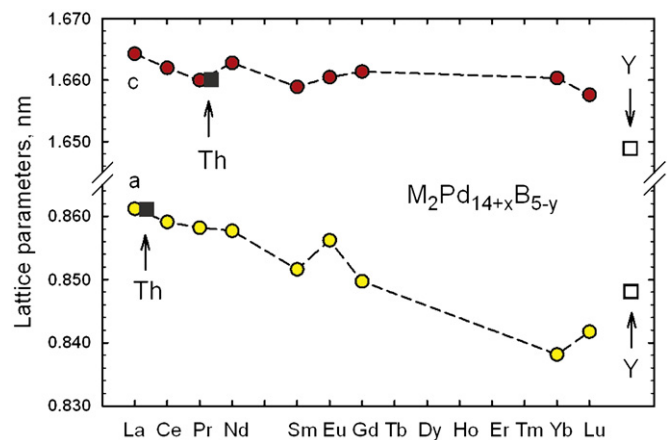


Fig. 15. Variations of the lattice parameters vs. rare earths in $\text{M}_2\text{Pd}_{14}\text{B}_5$ closed and open squares correspond to the lattice parameters of Th- and Y-compounds, respectively.

received are characterized by an upturn at low temperature and a maximum around 75 K. While the former is supposed to be a signature of a low temperature magnetic instability (below the experimental limit), the latter is attributed to crystalline electric field (CEF) effects. A Schottky curve adjusted to the experimental data reveals a doublet at 130 K and a quasi-quartet at 290 K above the ground state doublet. Integrating C_{mag}/T over T , the resulting magnetic entropy is presented in Fig. 17b. The limit of $2R \ln 8$ was not reached at the highest temperature measured.

The temperature dependent electrical resistivity of $\text{Yb}_2\text{Pd}_{14}\text{B}_5$ is shown in Fig. 18 together with the resistivity of $\text{Lu}_2\text{Pd}_{14}\text{B}_5$. Obviously, the latter shows metallic behavior in the entire temperature range; however, the negative curvature of $\rho(T)$

temperatures: $T_{E1}=116\text{ K}$, $T_{E2}=207\text{ K}$ and $T_{E3}=455\text{ K}$ with weights of $c_1=11$, $c_2=29$ and $c_3=20$, respectively. To compare the Debye temperature derived from the fit with the one derived at low temperatures, the former has to be multiplied by $n^{1/3}=2.76$, arriving at $\theta_D^{\text{corr}}=243\text{ K}$.

Analyzing the magnetic contribution to the specific heat of $\text{Yb}_2\text{Pd}_{14}\text{B}_5$, C_{mag} can be revealed as a difference of heat capacities of $\text{Yb}_2\text{Pd}_{14}\text{B}_5$ and $\text{Lu}_2\text{Pd}_{14}\text{B}_5$, i.e., $C_{\text{mag}}=C_p(\text{Yb})-C_p(\text{Lu})$. The data

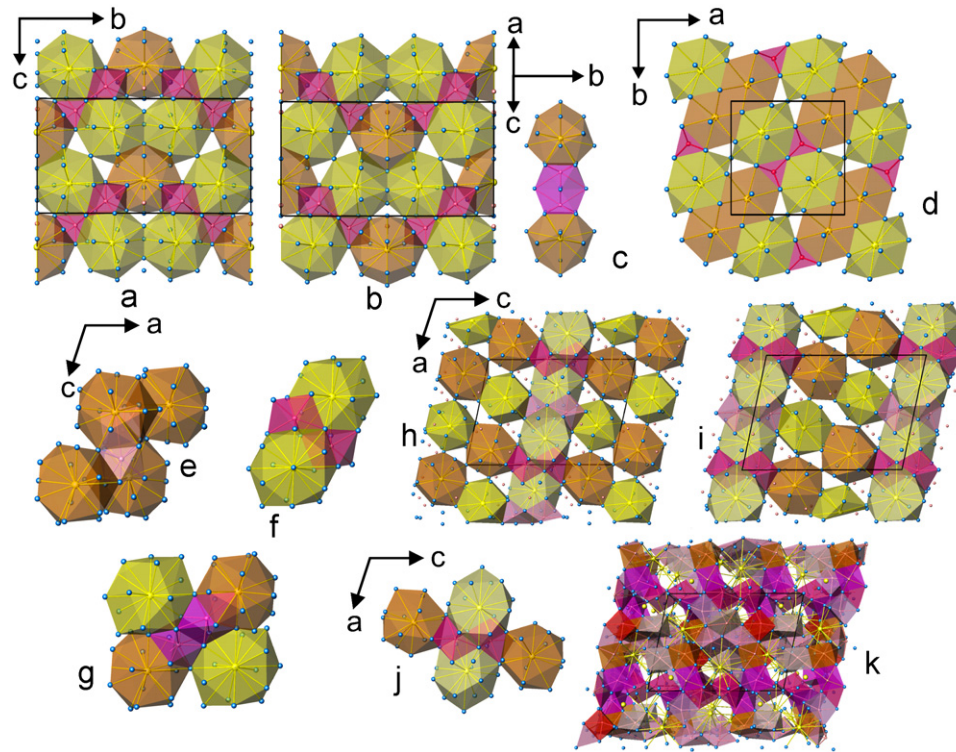


Fig. 16. Structural relationships in $\text{La}_6\text{Pd}_{47-x}\text{B}_6$, $\text{CePd}_8\text{B}_{2-x}$, $\text{La}_3\text{Pd}_{25-x}\text{B}_{8-y}$ and $\text{Yb}_2\text{Pd}_{14-x}\text{B}_5$. Arrangement of lanthanum and B1 coordination polyhedra in $\text{La}_6\text{Pd}_{47-x}\text{B}_6$: projections along [100], slabs at $x \approx 1/4$ (a), $x \approx 3/4$ (b). Aggregation of La2 and B2 polyhedra in $\text{La}_6\text{Pd}_{47-x}\text{B}_6$ (c). Structure of $\text{Nd}_2\text{Fe}_{14}\text{B}$ (d). Arrangement of coordination polyhedra in the structure of $\text{CePd}_8\text{B}_{2-x}$: Ce1B1 (e), Ce2B3 (f), Ce1Ce2B2 (g). Projection of $\text{La}_3\text{Pd}_{25-x}\text{B}_{8-y}$ along [010]: slabs at $y \approx 0$ (h), $y \approx 1/2$ (i). Linkage of La1La2B1 atoms in the structure of $\text{La}_3\text{Pd}_{25-x}\text{B}_{8-y}$ (j). Arrangement of B polyhedra in the structure of $\text{La}_3\text{Pd}_{25-x}\text{B}_{8-y}$ (k).

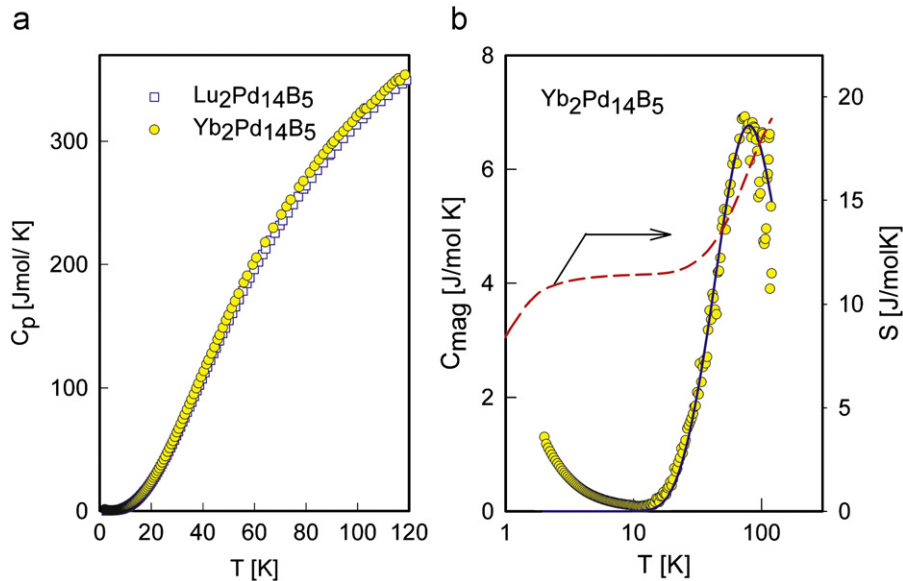


Fig. 17. (a) Temperature dependent specific heat C_p of $\text{Yb}_2\text{Pd}_{14}\text{B}_5$ and $\text{Lu}_2\text{Pd}_{14}\text{B}_5$ plotted as C_p vs. T (left axis). (b) Magnetic contribution of the specific heat $C_{\text{mag}}(T)$ of $\text{Yb}_2\text{Pd}_{14}\text{B}_5$ plotted as C_{mag} vs. T . The dashed line represents the magnetic entropy $S_{\text{mag}}(T)$ and refers to the right axis.

does not evidence a simple behavior. Besides this, $\text{Lu}_2\text{Pd}_{14}\text{B}_5$ exhibits rather large overall resistivity values as derived from a residual resistivity $\rho_0 = 210 \mu\Omega \text{ cm}$. Moreover the system shows a tendency to saturation as a consequence of the strong curvature of $\rho(T)$. The temperature dependence of the resistivity was described by the Bloch–Grüneisen formula modified by the model of Mott and Jones [55], accounting for scattering of conduction electrons on rather localized d -electrons. On the assumption of spherical s - and d -bands as well as Debye phonons

this s - d scattering process is responsible for a characteristic T^3 term at elevated temperatures ($T > \theta_D$). From this model a Debye temperature of 230 K is obtained and the Mott–Jones pre-factor amounts to roughly $1 \times 10^{-6} \mu\Omega \text{ cm K}^{-3}$. On the other hand, the parallel resistance model, generally used for materials with large absolute resistivities, does not fit properly.

In general, physics of Yb compounds is governed from a balance of the Kondo effect, the RKKY interaction and CEF effects. Distinct hints to the Kondo effect in $\text{Yb}_2\text{Pd}_{14}\text{B}_5$ are obvious from

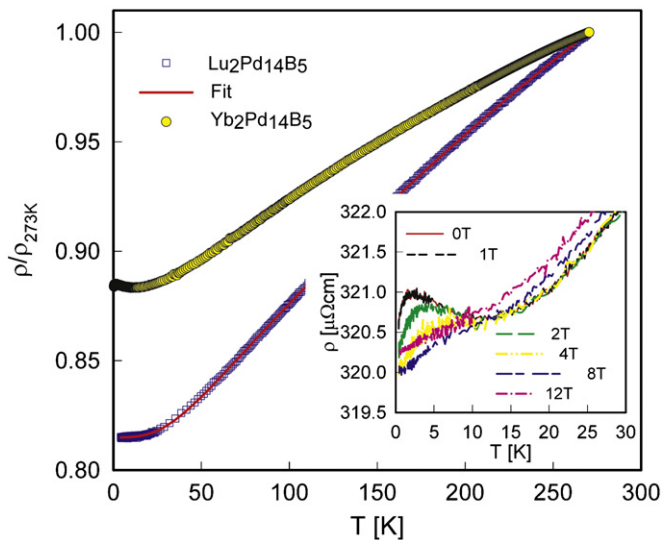


Fig. 18. Temperature dependent electrical resistivity ρ of $\text{Yb}_2\text{Pd}_{14}\text{B}_5$ and $\text{Lu}_2\text{Pd}_{14}\text{B}_5$ plotted in a normalized representation $\rho(T)/\rho(273)$. The inset shows low temperature resistivity data for $\text{Yb}_2\text{Pd}_{14}\text{B}_5$ at magnetic fields up to 12 T.

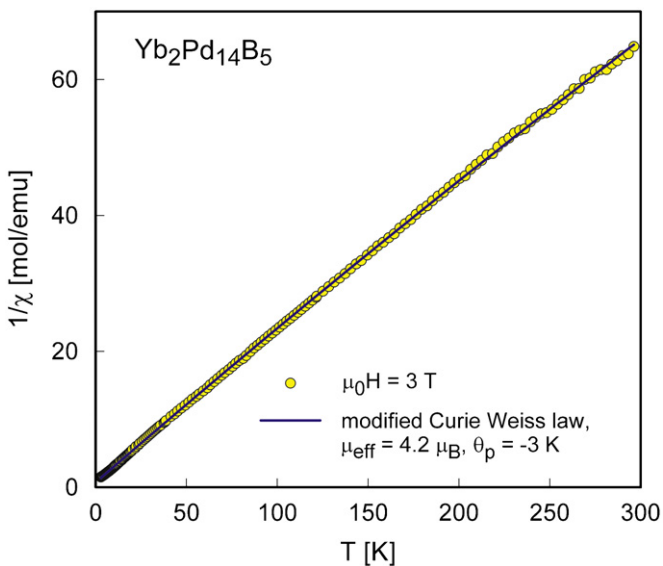


Fig. 19. Temperature dependent magnetic susceptibility χ of $\text{Yb}_2\text{Pd}_{14}\text{B}_5$, plotted as $1/\chi$ vs. T . Data are taken at 3 T. The solid line corresponds to a least squares fit to the experimental data in terms of a modified Curie–Weiss law.

the temperature dependent resistivity $\rho(T)$. The most important characteristics found at zero field are a negative logarithmic slope of $\rho(T)$ below about 12 K and a maximum at 2 K. While the former refers to Kondo interactions in the CEF ground state, the latter can be considered as a signature of coherence originated from the periodic arrangement of the Yb ions in $\text{Yb}_2\text{Pd}_{14}\text{B}_5$. The decrease of the resistivity below 2 K might result from the onset of long-range magnetic order, in agreement with the heat capacity data. The application of external magnetic fields causes an initial decrease of the electrical resistivity as well as a shift of the low temperature maximum to higher temperatures until it becomes totally suppressed at 8 T (see inset Fig. 18). These observations are typical features of Kondo lattices where the quenching of Kondo interaction by external magnetic field depletes the scattering intensity and thus reduces $\rho(T)$.

The magnetic configuration of $\text{Yb}_2\text{Pd}_{14}\text{B}_5$ can be proven by susceptibility measurements $\chi(T)$, for which the data of a 3 T run are shown in Fig. 19. A phase transition, in agreement with specific heat and electrical resistivity is not present above 2 K. To quantitatively account for temperatures above 20 K, a fit according to the modified Curie–Weiss law was employed, yielding a temperature independent Pauli-like susceptibility $\chi_0 \cong 1 \times 10^{-3}$ emu/mol, an effective moment $\mu_{\text{eff}} = 4.2 \mu_{\text{B}}$ and the Curie temperature $\theta_{\text{p}} = -3$ K. The effective moment is close to the theoretical value associated with the Yb^{3+} state, i.e., $4.54 \mu_{\text{B}}$, favoring the $4f^{13}$ electronic configuration as ground state of the Yb ions. The small negative paramagnetic Curie temperature hints at antiferromagnetic correlations, in line with a possible antiferromagnetic ground state.

4. Conclusions

Phase relations in the Ce–Pd–B and Yb–Pd–B systems at 850 °C were determined from X-ray powder diffraction of alloys annealed at 850 °C in the concentration ranges up to 45 and 33 at% of Ce and Yb, respectively. Two extended homogeneity fields, $\text{CePd}_8\text{B}_{2-x}\text{Ce}_3\text{Pd}_{25-x}\text{B}_{3-y}$ and CePd_3B_x were found to exist in equilibrium. CePd_3 was established to incorporate up to 13 at% of B from X-ray powder diffraction; the unit cell parameters of CePd_3B_x reach their maximum at $x = 0.25$. The crystal structure of $\text{CePd}_8\text{B}_{2-x}$ ($x = 0.46$ and 0.32) (own structure type, $C2/c$ space group) was studied by single crystal X-ray diffraction. The continuous transition from $\text{CePd}_8\text{B}_{2-x}$ to $\text{La}_3\text{Pd}_{25-x}\text{B}_{8-y}$ -type structure within the homogeneity field on progressing from the boron-poor to boron-rich members was revealed from Rietveld refinement of X-ray powder diffraction data. One more new ternary phase was found in the palladium rich region; however, due to the lack of good quality single crystal, the structure of the new compound ($\tau_1\text{-Ce}_6\text{Pd}_{47-x}\text{B}_6$ ($C2/m$ space group, $a = 1.03594(2)$ nm, $b = 1.80782(3)$ nm, $c = 1.01997(2)$ nm, $\beta = 108.321(1)^\circ$) was determined from Rietveld refinement of X-ray powder diffraction data applying the structural model obtained from $\text{La}_6\text{Pd}_{47-x}\text{B}_6$ ($x = 0.19$) single crystal (new structure type, $C2/m$ space group, $a = 1.03988(2)$ nm, $b = 1.81941(5)$ nm, $c = 1.02418(2)$ nm, $\beta = 108.168(1)^\circ$). $\text{Ce}_6\text{Pd}_{47-x}\text{B}_6$, $\text{CePd}_8\text{B}_{2-x}$ and $\text{La}_3\text{Pd}_{25-x}\text{B}_{8-y}$ structures exhibit the fragments common with $\text{Nd}_2\text{Fe}_{14}\text{B}$ and $\text{Nd}_2\text{Pd}_{14+x}\text{B}_{5-y}$.

The ternary compound $\tau_1\text{-Yb}_2\text{Pd}_{14-x}\text{B}_5$ ($x = 0.4$) ($I4_1/amd$ space group) was detected to be in equilibrium with YbPd_3B_x , YbB_6 , Pd_5B_2 and Pd_3B in the Yb–Pd–B system. The isotypic compound structurally related to $\text{Y}_2\text{Pd}_{14}\text{B}_5$ was observed with Lu. In the course of this study, the attempts to determine the structures of unknown compounds in the binary Yb–Pd system were undertaken; however, a good quality single crystal was obtained only for the Yb_5Pd_2 compound. In agreement with the literature data, the compound forms with a Mn_5C_2 -type. The refined atomic coordinates slightly deviate from those reported in the literature from photograph method but the atomic position of Pd atom was found to be occupied for 96.9% leading to a composition $\text{Yb}_5\text{Pd}_{1.94}$.

Physical properties derived for $\text{Yb}_2\text{Pd}_{13.6}\text{B}_5$ are characterised by an almost 3+ state of the Yb ion, leading to long range magnetic order below 2 K. The Kondo- and CEF effects control the paramagnetic temperature domain.

Acknowledgments

Research supported by Austrian National Science Foundation FWF projects 18054 and M1067-N20.

Appendix A. Supplementary material

Supplementary data associated with this article can be found in the online version at doi:10.1016/j.jssc.2010.02.016.

References

- [1] E. Bauer, G. Hilscher, H. Kaldarar, H. Michor, E.W. Scheidt, P. Rogl, A. Griбанov, Yu. Seropegin, J. Magn. Magn. Mater. 310 (2007) e73.
- [2] O.L. Sologub, J.R. Hester, P.S. Salamakha, E. Leroy, C. Godart, J. Alloys Compd. 337 (2002) 10.
- [3] T. He, Q. Huang, A.P. Ramirez, Y. Wang, K.A. Regan, N. Rogado, M.A. Hayward, M.K. Haas, J.S. Slusky, K. Inumara, H.W. Zandbergen, N.P. Ong, R.J. Cava, Nature 411 (2001) 54.
- [4] E. Bauer, G. Hilscher, H. Michor, C. Paul, E.W. Scheidt, A. Grybanov, Yu. Seropegin, H. Noel, M. Sigrist, P. Rogl, Phys. Rev. Lett. 92 (2004) 027003 1.
- [5] A. Griбанov, A. Grytsiv, E. Royanian, P. Rogl, E. Bauer, G. Giester, Yu. Seropegin, J. Solid State Chem. 181 (2008) 2964.
- [6] R. Schaak, M. Avdeev, W.-L. Lee, G. Lawes, J. Jorgensen, N. Ong, A. Ramirez, R. Cava, J. Solid State Chem. 177 (2004) 1244.
- [7] S.K. Dhar, S. Malik, R. Vijayaraghavan, Mater. Res. Bull. 16 (1981) 1557.
- [8] S.K. Dhar, K.A. Gschneidner Jr., C.D. Bredl, F. Steglich, Phys. Rev. B 39 (4) (1989) 2439.
- [9] J.P. Kappler, M.J. Besnus, E. Beaurepaire, A. Meyer, J. Sereni, G. Nieva, J. Magn. Magn. Mater. 47–48 (1985) 114.
- [10] M. Housliar, D. Androja, B. Rainford, Physica B 223–224 (1996) 268.
- [11] G. Wandahl, A.N. Christensen, Acta Chem. Scand. 43 (1989) 296.
- [12] J.R. Thomson, J. Less-Common Met. 13 (1967) 307.
- [13] T. Bretschneider, H.J. Schaller, Z. Metallk. 81 (1990) 84.
- [14] R. Lackner, E. Bauer, P. Rogl, Physica B 378–380 (2006) 835.
- [15] C. Loison, A. Leithe-Jasper, H. Rosner, Phys. Rev. B 75 (2007) 205135 1.
- [16] E. Royanian, E. Bauer, H. Kaldarar, A. Galatanu, R.T. Khan, G. Hilscher, H. Michor, M. Reissner, P. Rogl, O. Sologub, G. Giester, A. Pereira-Goncalves, J. Phys. Condens. Matter 21 (2009) 305401.
- [17] O. Sologub, P. Rogl, A. Grytsiv, G. Giester, J. Phys. Conf. Ser. 176 (2009) 012007.
- [18] Nonius Kappa CCD, Program Package COLLECT, DENZO, SCALEPACK, SORTAV, Nonius Delft, The Netherlands.
- [19] G.M. Sheldrick, Acta Crystallogr. A 64 (2008) 112.
- [20] G.M. Sheldrick, SHELXL-97, program for crystal structure refinement, University of Göttingen, Germany, Windows version by McArdle, National University of Ireland, Galway, 1997.
- [21] T. Roisnel, J. Rodriguez-Carvalaj, in: Materials Science Forum, Proceedings of the European Powder Diffraction Conference (EPDIC 7), 2000, p. 118.
- [22] T.B. Massalski, Binary Alloy Phase Diagrams, second ed., ASM International, Materials Park, OH, 1990.
- [23] P. Villars, L.D. Calvert, Pearson's Handbook of Crystallographic Data for Intermetallic Phases, second ed., ASM International, Materials Park, OH, 1991.
- [24] Y. Sakamoto, K. Takao, M. Ohmaki, J. Less-Common Met. 162 (1990) 343.
- [25] H. Okamoto, Desk Handbook Phase Diagrams for Binary Alloys, ASM International, Materials Park, OH, 2000.
- [26] A. Lipatov, A. Griбанov, A. Grytsiv, P. Rogl, E. Murashova, Yu. Seropegin, G. Giester, K. Kalmykov, J. Solid State Chem. 182 (2009) 2497.
- [27] N. Kuwano, K. Umeo, K. Yamamoto, M. Itakura, K. Oki, J. Alloys Compd. 181 (1992) 61.
- [28] D.A. Smith, I.P. Jones, J.R. Harris, J. Mater. Sci. Lett. 1 (1982) 463.
- [29] K. Zhang, L.L. Chen, X. Huaxue, Acta Chem. Sinica 47 (1989) 592.
- [30] J.P. Kappler, M.J. Besnus, P. Lehmann, A. Meyer, J. Sereni, J. Less-Common Met. 111 (1985) 261.
- [31] A. Palenzona, A. Iandelli, J. Less-Common Met. 34 (1974) 121.
- [32] D. Rossi, R. Ferro, R. Marazza, J. Less-Common Met. 40 (1975) 345.
- [33] J.D. Speight, I.R. Harris, G.V. Raynor, J. Less-Common Met. 16 (1968) 164.
- [34] K. Takao, Y. Sakamoto, T. Araki, H. Kohzuma, J. Alloys Compd. 193 (1993) 41.
- [35] Y. Sakamoto, F.L. Chen, M. Kinoshita, M. Minamikawa, J. Alloys Compd. 192 (1993) 141.
- [36] I.R. Harris, G.V. Raynor, J. Less-Common Met. 9 (1965) 263.
- [37] I.R. Harris, G.V. Raynor, C.J. Winstanley, J. Less-Common Met. 12 (1967) 69.
- [38] A. Iandelli, A. Palenzona, Rev. Chim. Miner. 10 (1973) 303.
- [39] A. Iandelli, G.L. Olcese, A. Palenzona, J. Less-Common Met. 76 (1980) 317.
- [40] P. Rogl, in: G. Effenberg (Ed.), Phase Diagrams of Ternary Metal–Boron–Carbon Systems, ASM, Ohio, USA, 1998, p. 234.
- [41] T.G. Berger, Ph.D. Thesis, University of Stuttgart, Bericht Nr. 164, 2005.
- [42] E. Parthé, L. Gelato, B. Chabot, M. Penzo, K. Censual, R. Gladyshevskii, TYPX—Standardized Data and Crystal Chemical Characterization of Inorganic Structure Types, Springer-Verlag, Berlin, Heidelberg, 1994.
- [43] P. Rogl, in: J.J. Zuckerman (Ed.), Inorganic Reactions and Methods, vol. 13, VCH-Publications Inc., New York, 1991, pp. 85–167 (Chapter 6).
- [44] H. Bärnighausen, U. Müller, Symmetriebeziehungen zwischen den Raumgruppen als Hilfsmittel zur straffen Darstellung von Strukturzusammenhängen in der Kristallchemie, University of Karlsruhe and University/GH Kassel, Germany, 1996.
- [45] Yu.B. Kuz'ma, O.M. Dub, V.A. Bruskov, N. Chaban, L.V. Zavalii, Kristallografiya 33 (1988) 841.
- [46] Yu.B. Kuz'ma, V. Babizhetskyy, I. Veremchuk, N. Chaban, J. Solid State Chem. 177 (2004) 425.
- [47] P.S. Salamakha, A.P. Goncalves, O.L. Sologub, M. Almeida, J. Alloys Compd. 360 (2003) 61.
- [48] T. Gloviak, S.V. Orishchin, I.B. Gubich, N.F. Chaban, Yu.B. Kuz'ma, Sov. Phys. Crystallogr. 34 (4) (1989) 602.
- [49] O.M. Dub, Y.B. Kuz'ma, Inorg. Mater. 23 (1987) 42.
- [50] P.S. Salamakha, O.L. Sologub, J.R. Hester, C. Rizzoli, A.P. Goncalves, M. Almeida, J. Alloys Compd. 439 (2007) 162.
- [51] Yu.B. Kuz'ma, Crystal Chemistry of Borides, Vyscha Shkola Press, Lvov, 1983.
- [52] H. Boller, H. Oesterreicher, J. Less-Common Met. 103 (1984) L5.
- [53] P. Salamakha, O. Sologub, A.P. Goncalves, M. Almeida, J. Alloys Compd. 360 (2003) 131.
- [54] W. Jung, M. Weltzer, Z. Kristallogr. 196 (1991) 169.
- [55] J.C.H. Chiu, Phys. Rev. B 13 (1976) 1507.